Revision 2

Modified magnetite and hydrothermal apatite in banded iron-formations and its implications for high-grade Fe mineralisation during retrogressive metamorphism

Kangxing Shi[1], Changming Wang[1, *], Leon Bagas[1, 2], and Hongyu Duan[1]

[1] *State Key Laboratory of Geological Processes and Mineral Resources, School of Earth Sciences and Resources, China University of Geosciences, Beijing 100083, China*

[2] *Xi'an Center of China Geological Survey, Xi'an 710054, China*

* Corresponding author: Changming Wang, E-mail: wangcm@cugb.edu.cn

Abstract

Modified magnetite and hydrothermal apatite in banded iron-formations (BIFs) are ideal minerals for studying hydrothermal and metamorphic processes, and are applied to linking with high-grade Fe mineralisation and metamorphism in iron deposits hosted by BIFs. This study investigates the geochemical composition of modified magnetite and hydrothermal apatite, and *in situ* U–Pb geochronology on apatite from the Huogezhuang BIF-hosted Fe deposit in the northeastern China. The magnetite in metamorphosed BIF is modified, locally fragmented and forms mm- to μm-scale bands. The apatite is present surrounding or intergrowing with magnetite, and has corroded surfaces and contains irregularly impurities and fluid inclusions, indicating that it has been partly hydrothermal altered. Original element compositions (e.g., Fe, Al, Ti, K, Mg and Mn) of magnetite in BIFs have been modified during high-grade Fe mineralisation and retrogressive metamorphism with the temperature reduction and acids. The hydrothermally altered apatite has been relatively reduced in Ca, P, F, La, Ce, Nd, δCe, δEu, and total REEs contents compared to non-altered apatite. The magnetite and apatite in low-grade BIFs are poorer in FeO_T than those of from the high-grade Fe ores, indicating that Fe is remobilised during the transition from BIFs to high-grade Fe ores. The magnetite and apatite in high-grade Fe ores are overgrown by greenschist-facies minerals formed during retrograde metamorphism, suggesting that the high-grade Fe mineralisation may be related to retrogressive metamorphism. *In situ* U–Pb geochronology of apatite intergrown with magnetite and zircon LA–ICP–MS U–Pb dating at Huogezhuang deposit reveal that the BIF-hosted magnetite was altered and remobilised at ca. 1950–1900 Ma, and deposition

of the BIF began during the Late Neoarchaean. The changes of elements in the modified magnetite, and different geochemical compositions of the altered and unaltered apatite confirm that the modified magnetite and hydrothermal apatite can be effective in tracing high-grade Fe mineralisation and retrogressive metamorphism in BIFs.

Keywords: Banded iron-formation; Apatite; Magnetite; High-grade iron ore; Mineralisation and metamorphism; Huogezhuang deposit

Introduction

The banded iron-formations (BIFs)-hosted iron deposits are one of the important iron resources, with the quantity of both exploitation and resource reserve ranking as the first in the world (Zhang et al. 2014a, 2014b, 2021; Li et al. 2015a). The high-grade Fe ores in China only account for less than 2%, which is significantly different from other countries where the high-grade ores are mainly BIFs-type iron ores (Zhang et al. 2014a, 2014b, 2021; Li et al. 2015a; 2016, 2019). Most of them are high-grade hematite deposits, with multistage fluids moved downward and leached the BIFs along deformation structures, including the Hamersley Province in Australia and the Quadrilátero Ferrífero region in Brazil (Hagemann et al., 2016; Sheppard et al. 2017a, 2017b; Rasmussen and Muhling 2018; Li et al. 2019). However, the high-grade Fe ores in China are related to magnetite deposits hosted by BIFs and have undergone retrograde metamorphism with fluid metasomatism (Li and Zhang 2013; Lan et al. 2019a, 2019b; Green et al. 2020). High-grade magnetite deposits hosted by BIFs have been mined mainly in the Anshan–Benxi area and eastern Hebei province-Miyun Terrane of the North China (Wan et al. 2018; Wang et al. 2018).

Magnetite and associated minerals (such as apatite, xenotime, and monazite intergrown with magnetite) are ideal provenance indicators for genetic studies of the Archaean to Early Palaeoproterozoic BIFs (Lan et al. 2019a, 2019b). Compositions of these minerals have been successfully used for tracing the genesis of BIFs and enrichment mechanism of the BIFs-related high-grade Fe ores (e.g., James 1954; Gross 1980, 1983; Clout and Simonson 2005; Dai et al. 2014, 2017; Li et al. 2019; Aftabi et al. 2021;

Pirajno and Yu 2021). Most BIFs have undergone retrograde metamorphism at various grades after diagenesis (Klein 1978; Klein and Beukes 1993; Mücke et al. 1996; Konhauser et al. 2009; Li and Zhang 2013; Lan et al. 2019a, 2019b; Green et al. 2020). Magnetite (an abundant and widespread oxide mineral) and apatite (a common tracer mineral) in BIFs are ideal minerals to study the hydrothermal and metamorphic processes, and the genesis of high-grade iron ores of BIFs (Cook et al. 2016; Andersson et al. 2019; Xing et al. 2020). The hydrothermal alteration and metamorphism can modify the structure of magnetite and alter the apatite in BIFs. Some trace elements (e.g., Mg, Mn, Al, Cr, V, and Ti) could partially exchange with Fe in magnetite (Skublov and Drugova 2003; Klein 2005; Zhang et al. 2011; Angerer et al. 2013, 2016; Deng et al. 2017; Lan et al. 2019a, 2019b; Green et al. 2020), and compositions of the apatite intergrowing or coexisting with magnetite would be partly or completely changed (Piccoli and Candela 2002; Andersson et al. 2019; Xing et al. 2020; Gillespie et al. 2021). Previous studies have found that the hydrothermally altered apatite has been relatively depleted in Sr from the BIFs in Pääkkö of Finland and Hamersley Basin of Australia (Alibert 2016; Azadbakht et al. 2018; Andersson et al. 2019; Wudarska et al. 2020).

Some previous studies have confirmed that the high-grade Fe ores attributed to hypogene hydrothermal enrichment of BIFs (Li et al. 2019, 2020; Sun et al. 2020). The two contentious models proposed for the detailed process of high-grade Fe mineralisation by hydrothermal and metamorphic events in the North China are: (1) remobilisation and re-precipitation of iron, i.e., iron is dissolved and migrated by hydrothermal fluids and then

precipitated under favourable conditions (Yang et al. 2019; Zhang et al. 2021); and (2) desiliconization and iron enrichment, i.e., silica is removed from the BIFs by fluids and the residual magnetite remains in situ to form high-grade Fe ores (Zhang et al. 2014a, 2014b, 2021; Li et al. 2015a). Furthermore, *in situ* U–Pb geochronology on monazite and xenotime intergrown with magnetite and hematite has been attempted to date the high-grade BIF-hosted mineralisation (Li et al. 2015, 2016, 2019; Zi et al. 2015, 2018). Modified magnetite and hydrothermal apatite might offer insights into the intensity of chemical exchanges during the metamorphism of BIFs, and the metallogenic process of high-grade Fe ores (Urban et al. 1992; Duuring et al. 2012, 2018; Bouzari et al. 2016; Adomako-Ansah et al. 2017; Soares et al. 2017; Kumar et al. 2018; Chen et al. 2019; Lan et al. 2019a, 2019b; Green et al. 2020; Xing et al. 2020). However, how the original compositions in magnetite and apatite from BIFs have been modified in such process and its genetic link to high-grade Fe mineralisation remain unclear.

The Huogezhuang BIF-hosted iron deposit is a large metamorphosed deposit with a resource of 180 Mt and average 26.7% Fe. The deposit is located in the Miyun Terrane of the northeastern North China Block (NCB; Figs. 1 and 2; Shi and Shi 2016; Fang et al. 2017). The type of the BIF deposit, source of the iron, age of the deposition and mineralisation are previous studied. (1) The protoliths of the Huogezhuang BIF are modified during granulite- to amphibolite-facies metamorphism and retrogressed at greenschist-facies (Shi and Shi 2016). (2) The mineralised zone includes low-grade BIF and high-grade Fe ores (Fig. 2a; Shi and Shi 2016). (3) The magnetite in metamorphosed BIF is modified and locally fragmented, and the

apatite is present surrounding or intergrowing with magnetite. These features make the Huogezhuang BIF-hosted Fe deposit an ideal target for studying the modification and remobilisation of iron, and hydrothermal alteration during the retrogressive metamorphism and high-grade Fe mineralisation.

In this paper, we present mineralogy, laser-ablation inductively-coupled-plasma mass-spectrometry (LA–ICP–MS) and electron probe micro-analysis (EPMA) of apatite and magnetite, and *in situ* apatite and zircon U–Pb geochronology from the Huogezhuang Fe deposit in the northeastern China. Systematic element compositions have been analysed in modified magnetite and hydrothermal apatite to reveal the high-grade Fe mineralisation and retrogressive metamorphism of the Huogezhuang BIF-hosted iron deposit. Apatite *in situ* U–Pb geochronology was used to date the hydrothermal and metamorphic events.

Geological background

The NCB associated with Archaean world-class metallogeny is a topic of widespread interest (Kusky et al. 2007, 2016; Zhai and Santosh 2011; Zhao and Zhai 2013; Zhai et al. 2005, 2015; Wang et al. 2015, 2016, 2018; Deng et al. 2017; Santosh et al. 2020). The continental-size region has been subdivided into the Western and Eastern zones separated by the ca. 1950–1850 Ma Trans-North China Orogen (Zhao et al. 2001; Kusky and Li 2003; Zhao 2007; Santosh 2010; Santosh et al. 2013), and Proterozoic and Phanerozoic basins (Fig. 1). Both zones include Neoarchaean BIF mineralisation (Diwu et al. 2010, 2014; Zhai and Santosh 2011; Tang and Santosh 2018; Zhai et al. 2020; Duan et al. 2021). The NCB records a long and complex geological history spanning almost continuously from the

147 Archaean to Cenozoic, including magmatism, sedimentation, metamorphism,
148 and multiple deformation events extending into the Mesozoic (Bagas et al.
149 2020). Zhai and Santosh (2011) proposed that the NCB was an amalgamation
150 of the Archaean Qianhuai, Jiaoliao, Xuhuai, Xuchang, Alashan, Jining, and
151 Ordos microblocks, which were strongly deformed metamorphosed up to
152 granulite-facies. The proposed microblocks consist of orthogneiss,
153 amphibolite and lenses of BIF-bearing metavolcanic and metasedimentary
154 rocks (Zhai et al. 2015; Tang and Santosh 2018; Duan et al. 2021). The BIF-
155 hosted Fe deposits in the Eastern Zone are located at the Jianping, northern
156 Liaoning, eastern Hebei and western Shandong provinces, and include the
157 Anshan, Wuyang, and Miyun deposits (Fig. 1). The source of the iron is
158 principally Neoarchaean to Early Palaeoproterozoic BIF (Fig. 1; e.g., Shen et
159 al. 2011).

160 The Miyun Terrane is located to the north of Beijing, where Archaean
161 granulite- to amphibolite-facies orthogneiss and paragneiss crop out (Fig. 1;
162 Wan et al. 2012; Shi and Shi 2016; Fang et al. 2017; Deng et al. 2018;
163 Santosh et al. 2020). The orthogneiss includes monzogranite, granodiorite,
164 trondhjemite, tonalite. The supracrustal rocks form NE-trending belts
165 consisting of ultramafic to felsic metavolcanic rocks, and paragneiss (included
166 metamorphosed BIF) intruded by Palaeoproterozoic mafic dykes (Shi and Shi
167 2016; Fang et al. 2017; Tang et al. 2019; Santosh et al. 2020). The
168 metamorphosed supracrustal rocks are assigned to the Miyun and Sihetang
169 complexes (Shi and Shi 2016; Fang et al. 2017; Tang et al. 2019; Santosh et
170 al. 2020). The Sihetang Complex is informally subdivided into the Yangpodi,
171 Songyingzi, Xiwanzi and Shanshenmiao units (Shi and Shi 2016; Fang et al.

2017), and the Miyun Complex is informable subdivided into the Shachang, Weiziyu, and Dacao units (Tang et al. 2019; Santosh et al. 2020). The Miyun Complex records multiple magmatic events, including Archaean to Palaeoproterozoic orthogneiss, supracrustal rocks, metapyroxenite and metagabbro, mafic dykes and porphyritic monzogranite, and Mesozoic monzogranite (Shi and Shi 2016; Fang et al. 2017; Tang et al. 2019; Santosh et al. 2020). The tectonic structures are complex and include multiple generations of folds and faults, including the Banchengzi, Qifengcha, Shicheng and Huolangyu faults. The faults trend northeastward and constitute the boundary of complexes (Fig. 1; Santosh et al. 2020).

The Huogezhuang deposit is an example of a large, metamorphosed BIF-hosted Fe deposit located in the Archaean Miyun Complex (Fig. 2; Zhang et al. 2012; Shi and Shi 2016; Fang et al. 2017). The host rocks are orthogneiss, garnet-bearing gneiss and BIF metamorphosed at granulite- to amphibolite-facies and retrogressed at greenschist-facies (Shi and Shi 2016). The deposit is located at the intersection between E- and N-trending faults (Fig. 2). These structures are cross-cut by ENE-trending strike-slip faults (Fig. 2). The igneous rocks in the area are variably metamorphosed porphyritic monzogranite, gabbro and lamprophyre, and minor relatively later intermediate to felsic pegmatite veins and dykes that crosscut the deposit (Figs. 2 and 3a, b).

The mineralised zone averages 26.7% Fe, including low-grade BIF (~20.0% Fe) and high-grade Fe ores (~50.0% Fe), consisting of three lensoidal and sigma-shaped orebodies with a thickness reaching ~10 m and a total length of around 10 km (Fig. 2a; Shi and Shi 2016). The occurrence of

the high-grade Fe orebodies is roughly consistent with that of the BIFs, and there is a smooth transition from high-grade Fe ores to BIFs (Figs. 2 and 3c, e, f). The orebodies are bound by several normal faults (F1, F2, F3, F4) that dip 25°-45°SW and trend ~340° (Figs. 2 and 3a, b). The high-grade Fe ores are often close to the faults (Fig. 2). The orebodies are folded and locally form boudins (Figs. 2 and 3a, b). The Fe ores are mainly characterized by banded (BIFs) or massive (high-grade Fe ore) structure and granular texture (Fig. 3e, f). The mineralisation is hosted by interlayered granulite- to amphibolite-facies magnetite-bearing quartz mafic gneiss, and magnetite-bearing quartz amphibolite, which have retrogressed to greenschist-facies indicated by the presence of chlorite, epidote, allanite and titanite alteration (Fig. 4). The host sequence is interpreted as metamorphosed mafic volcanic and BIF units. The contact between the Fe-ore and garnet-bearing gneiss is rich in garnet and magnetite (Fig. 3c). The mineralisation and host rocks are altered by carbonate, chlorite, and titanite (Fig. 3c, d), and chlorite has also crystallised along the foliation in the wall rocks (Fig. 3b). The carbonate, chlorite and titanite alteration has significantly affected the orebodies and is indicative of a late greenschist-facies event.

Samples and methods

Samples

Samples of BIF and high-grade Fe ore were collected from the Central ore block at the Huogezhuang deposit for analyses. A brief summary of the field occurrence and petrography of the samples is given below. The BIF sample is dark grey to black, fine-grained, has a gneissic texture, and consists magnetite (~55 vol.%), quartz (~25 vol.%), hornblende (~5 vol.%),

clinopyroxene (~10 vol.%), apatite (~4 vol.%), and minor amounts of plagioclase, chlorite and epidote (up to 1 vol.%; Fig. 3e). The high-grade Fe ore sample is dark black, fine-grained, gneissic, and consists of magnetite (~65 vol.%), quartz (~15 vol.%), hornblende (~5 vol.%), clinopyroxene (~10 vol.%), apatite (~4 vol.%), and minor amounts of plagioclase, chlorite, and epidote (up to 1 vol.%; Fig. 3f).

The magnetite is fragmented (Fig. 4c). The apatite forms clusters or around and intergrowth with the magnetite and quartz, and contains irregularly minerals and fluid inclusions (Fig. 4g–i). Allanite, epidote and titanite have often crystallised around apatite grains (Fig. 4g–i).

Backscattered electron and cathodoluminescence imaging

Backscattered electron (BSE) and cathodoluminescence (CL) images were generated at the Beijing Research Institute of Uranium Geology using a Tescan GAIA3 scanning electron microscope (SEM) with a focused ion beam (FIB) and equipped with an Oxford Instruments CL detector. Polished 50 μm thick sections were carbon coated (15–20 nm) and analysed at 10 keV with a beam current of 0.5 to 5 nA.

Electron probe micro-analysis and mapping

Mineral chemical concentrations and mapping were analysed using a JEOL JXA-8230 EPMA at the Beijing Research Institute of Uranium Geology. The electron microprobe was optimized for non-destructive, high-sensitivity spot analyses and element mapping in order to reduce sample damage and preserve the samples for additional analyses. The elements Ca, P, F, Cl, La, Ce, Sm, Nd, Gd, Ho, Yb, and Y were chosen for analyses. The operation conditions included an acceleration voltage of 15 keV, a beam current of 200

nA, a beam diameter of 5 μm, 300 s counting time on peak and 150 s on each background peak. High-sensitivity, low-resolution trace element mapping of one sample was carried out using a method of spot analyses, whereas counting times for Ca, P, F, Cl, La, Ce, Sm, Nd, Gd, Ho, Yb, and Y were reduced to 100 s on peak and 60 s off peak to decrease analysis time. The mapping consumed 12 hours of instrument time resulting in a small loss of sensitivity, based on 5 μm spot analyses within a 520 × 520 μm rectangle.

Apatite in situ U–Pb geochronology and trace elemental analysis

In situ LA–ICP–MS U–Pb geochronology of apatite was performed at the Nanjing Hongchuang Geological Exploration Technology Service Company. The Resolution SE model laser ablation system (Applied Spectra, USA) was equipped with a 193 nm ATL (ATLEX 300) excimer laser with spot sizes of 30 μm at 5 Hz and a fluence of 2 J/cm^2. The laser ablation system was coupled to an Agilent 7900 ICP–MS (Agilent, USA). Detailed tuning parameters were documented by Thompson et al. (2018). The Iolite software package was used for data reduction (Paton et al. 2010). Apatite Madagascar was used as a primary standard, and Apatite Durango was used as a secondary (McDowell et al. 2005). NIST 610 and ^{43}Ca were used to calibrate the trace element concentrations as external and internal standard samples, respectively.

Zircon U–Pb dating

Zircons were separated from crushed rock samples using standard heavy-liquid and magnetic methods at the Beijing Geo-Analysis Company, Limited. The CL images were obtained prior to analysis, to reveal internal zonation and enhance analytical targeting. Zircon samples were selected for LA–ICP–MS zircon U–Pb dating at the Mineral Laser Micro-Analysis

Laboratory, China University of Geosciences, Beijing. The zircon grains were ablated using a NewWave 193^{UC} ArF excimer laser with a 35 μm diameter laser spot, 8 Hz laser repetition rate, and laser energy of 8.5 J/cm^2. Isotopic intensities were measured using an Agilent 7900 quadrupole ICP–MS. The ablated material was carried in a high-purity helium gas into the ICP–MS. The integration time of Th is 10 ms, the integration time of U and ^{208}Pb is 15 ms, the integration time of ^{207}Pb is 30 ms, the integration time of ^{204}Pb and ^{206}Pb is 20 ms, and the integration time of all other elements is 6 ms. The international glass standard NIST 610 was used as the primary standard to calculate most elemental concentrations and to correct for instrument drift. The U–Pb isotope fractionation effects were corrected using the zircon 91500 as an external standard (Wiedenbeck et al. 2004). The zircon GJ-1 standard was used for data quality assessment (Jackson et al. 2004). Mass bias, laser-induced mass fractionation and instrument drift were corrected using ICPMSDataCal 10.2 (Liu et al. 2010).

Results

Magnetite and apatite texture

The metamorphosed BIF is commonly banded, fine-grained, and consists of quartz, magnetite, clinopyroxene, hornblende, plagioclase, and minor amounts of biotite and apatite (Fig. 4). The magnetite is modified and locally fragmented, subhedral to anhedral measuring ~1.5 mm across, and forms mm- to μm-scale bands (Fig. 4c). Subhedral to anhedral, 0.3-0.03 mm wide apatite commonly forms clusters or is present surrounding or intergrowing with magnetite and quartz, which is indicative of a contemporary mineralising event (Fig. 4d, e). The apatite grains have corroded surfaces and contain

297 irregularly impurities and fluid inclusions, and are overgrown by chlorite,
298 allanite, epidote, and titanite (Fig. 4g–i), showing partly hydrothermal
299 alteration features.

300 **Magnetite and apatite chemistry**

301 The geochemistry of the magnetite and apatite is listed in Supplementary
302 Tables S1–S2.

303 The magnetite grains from the BIF assay average 0.06 wt.% $Na_2O + K_2O$,
304 average 1.28 wt.% Al_2O_3, average 0.81 wt.% TiO_2, and average 90.29 wt.%
305 FeO_T (Supplementary Table S1; Fig. 5).

306 The magnetite grains from the high-grade Fe ore assay average 0.04 wt.%
307 $Na_2O + K_2O$, average 0.35 wt.% Al_2O_3, average 0.25 wt.% TiO_2, and average
308 92.98 wt.% FeO_T (Supplementary Table S1; Fig. 5).

309 The apatite grains in the samples of BIF and high-grade Fe ore have both
310 been partly hydrothermal altered and are characterised on Cl images by dark-
311 grey zones corresponding to alteration and light-grey apatite zones
312 representing non-altered areas (Figs. 6b, 7b and 8b). The altered apatite is
313 relatively reduced in La, Ce, Nd and total REEs compared with the non-
314 altered apatite (Supplementary Tables S1–S2).

315 **Apatite in situ U–Pb geochronology**

316 The apatite grains from the high-grade Fe ore (Sample D01B6) are light
317 brown, euhedral to subhedral, ranging up to 100 μm long with a length to
318 width ratio of ~2:1. Some of the apatite grains are partly rounded and decayed
319 (Fig. 9a). Thirteen analysed spots assay 0.1 to 6.6 ppm Th and 0.4 to 2.6 ppm
320 U with Th/U ratios of 0.4–2.7 (Supplementary Table S3), and yielded a lower

intercept age of 1902 ± 18 Ma with a 2σ error and MSWD value of 2.4 (Fig. 9a).

The apatite grains from the BIF sample (Sample D01B5) are light brown, euhedral to subhedral, range up to 200 μm long, and have a length to width ratio of 4:1. The apatite is partly rounded and decayed (Fig. 9b). Nineteen spots assay 0.2 to 5.3 ppm Th and 2.8 to 14.2 ppm U with a Th/U ratio of 0.04–0.37 (Supplementary Table S3), and yielded a lower intercept age of 1951 ± 29 Ma with a 2σ error and MSWD value of 2.5 (Fig. 9b).

Zircon U–Pb dating

Twenty-six zircons from the high-grade Fe ore (Sample D01B3) were U-Pb dated (Supplementary Table S4). The zircons are colourless or brownish, with a maximum length of 150 μm and a length to width ratio of 3:1 to 1:1 (Fig. 10a). Twenty-six analysed spots assay 7–234 ppm Th, and 14–599 ppm U with a Th/U value of 0.11–2.95. The analyses form three age groups within analytical error, with an upper intercept age of 2495 ± 64 Ma and a lower intercept age of 1849 ± 100 Ma (MSWD = 2.0; Fig. 10a). The first group yielded a weighted mean $^{207}Pb/^{206}Pb$ age of 2511 ± 47 Ma (MSWD = 2.1; Fig. 10a). The second group yielded a weighted mean $^{207}Pb/^{206}Pb$ age of 2226 ± 78 Ma (MSWD = 2.0; Fig. 10a). The third group yielded a weighted mean $^{207}Pb/^{206}Pb$ age of 1855 ± 43 Ma (MSWD = 1.5; Fig. 10a).

Twenty-eight zircons from the BIF sample (Sample D01B5) are colourless or brownish, with a maximum length of 120 μm and a length to width ratio of 2.5:1 to 1:1 (Fig. 10b). Twenty-eight analysed spots assay 57–320 ppm Th and 94–944 ppm U with a Th/U value of 0.33–3.73. Twenty-six analyses yielded an upper intercept age of 2496 ± 76 Ma, a lower intercept

age of 1969 ± 77 Ma (MSWD = 2.7), and a weighted mean $^{207}Pb/^{206}Pb$ age of 2497 ± 16 Ma (MSWD = 2.8; Fig. 10b). Another two analyses yielded weighted mean $^{207}Pb/^{206}Pb$ ages of 2883 ± 19 and 2084 ± 34 Ma (Fig. 10b).

The density probability plot in Fig. 10c highlights two major peaks at ca. 2500 and 1900 Ma.

Discussion

Ages of BIFs deposition and remobilisation

There have been many studies aiming to date BIF-hosted Fe deposits throughout the northeastern China and other terranes in the world using U–Pb zircon geochronological analyses (e.g., Klein 2005; Li et al. 2010, 2011, 2012, 2014, 2015a, 2015b; Shen et al. 2011, 2015; Zhang et al. 2012; Wang et al. 2014, 2015; Sheppard et al. 2017a, 2017b). Meso– to Neoarchean rocks of the Yilgarn Craton located in Western Australia consist of granite–greenstone lithologies and BIFs. The BIF metallogenic age is indirectly constrained to be ca. 2800–2600 Ma by the ages of syenogranitic to tonalitic orthogneiss and greenstones (e.g., Angerer et al. 2013; Haugaard et al. 2017; Soares et al. 2017; Rasmussen and Muhling 2018; Perring et al. 2020). The BIF–hosted Fe mineralisation in the NCB is hosted by the Meso- to Neoarchaean gneisses and supracrustal rocks. Zhang et al. (2012) proposed that the age of the peak deformation affecting BIF horizons in the region was ca. 2560–2520 Ma with the earliest BIF-hosted Fe deposit being Palaeoarchaean in age and the youngest was early Palaeoproterozoic dated at ca. 2400 Ma. Most of the BIFs in eastern Hebei Province were deposited in the Late Neoarchaean peaking at ca. 2600–2500 Ma, and there is only one BIF horizon in the area dated at ca. 3400 Ma (e.g., Zhang et al. 2012; Wang et al. 2018). The age of the BIFs

371 at the Anshan–Benxi area in the Liaoning Province is also Late Neoarchaean
372 dated at ca. 2550–2500 Ma, and one dated at ca. 3100 Ma (e.g., Wan et al.
373 2018; Wang et al. 2018). Wan et al. (2012) proposed that the BIF units in the
374 eastern NCB were formed between ca. 2550 and 2500 Ma. These ages,
375 however, only limit the upper and lower ages of the BIFs. The gneisses and
376 supracrustal rocks were deformed, metamorphosed at granulite- to
377 amphibolite-facies and retrograded to greenschist-facies during ca. 2500–
378 1800 Ma (Deng et al. 2017). These events might lead to the deformation,
379 metamorphism, and remobilisation of the Fe deposits hosted by BIFs (Shi et
380 al. 2019a).

381 This study focuses on a rare example of BIF in the Miyun Terrane. Shi
382 and Shi (2016), Fang et al. (2017) and Shi and Zhao (2017) documented that
383 the BIF units in the Miyun Terrane yielded LA–ICP–MS U–Pb zircon dates of
384 ca. 2550–2450 Ma, based on the dates obtained from BIF ore and the host
385 rocks. The granite, gneiss, amphibolite, and hornblendite in the Miyun Terrane
386 reveal emplacement ages from 2594 to 2496 Ma, and record metamorphic
387 events at ca. 2550, 2440, 1950 and 1820 Ma (Shi and Zhao 2017). In this
388 study, zircon U–Pb dating of the high-grade Fe ore and BIF sample from the
389 Huogezhuang deposit yields dates of ca. 2500–1850 Ma (Fig. 10a–c). Apatite
390 *in situ* U–Pb geochronology shows lower intercept ages of ca. 1950–1900 Ma
391 (Fig. 9). The results indicate that the Huogezhuang BIF-hosted iron deposit
392 formed ca. 2500 Ma, and was altered and remobilised during ca. 1950–1900
393 Ma. In addition, Li et al. (2019) described the Gongchangling BIF-hosted Fe
394 deposit in the Anshan-Benxi area of the northeastern NCB, and concluded
395 that the high-grade iron ore in this deposit formed at ca. 1860 Ma based on *in*

396 *situ* U–Pb geochronology of monazite and zircon. Sun et al. (2020) tested the
397 garnet from the altered wall rock of high-grade iron ore in the Gongchangling
398 BIF-hosted Fe deposit. These garnets yielded a Sm–Nd isochron age of 1888
399 ± 77 Ma, interpreted as the time of metamorphism in this area, which further
400 confirmed that the remobilisation of high-grade iron ore in the deposit was
401 later than the late Neoarchean. Li et al. (2020) reported an age of 1940 Ma
402 represented the metamorphic-hydrothermal monazite/xenotime growth after
403 deposition of the BIFs, based on *in situ* U-Pb geochronology of monazite and
404 xenotime intergrown with hematite from the Yuanjiacun BIF-hosted Fe deposit
405 in the central NCB. These ages are similar to the ca. 1950–1900 Ma date
406 mentioned above, which are coincident with the major regional metamorphic
407 events (1950–1850 Ma in the Miyun Terrane) and related to amalgamation of
408 the Western and Eastern zones of the NCB along the Trans-North China
409 orogen. Besides, the orebodies are bound by several normal faults and the
410 high-grade Fe ores are often close to the faults in the Huogezhung area (Fig.
411 2). The results may provide new clues to the age of BIFs and Fe
412 mineralisation in eastern NCB. The close relationship in time and space
413 between metamorphism of BIFs and host rocks in the Huogezhung area and
414 remobilisation of the Huogezhung BIF iron ores indicates a genetic link. The
415 metamorphism may induce a metamorphic-hydrothermal event and drive the
416 remobilisation of BIF iron. It is possible to be a potential for prospecting for
417 high-grade iron ores hosted by BIFs in the metamorphic region and faults.

418 **Modified magnetite and hydrothermal apatite in BIFs**

419 Magnetite is an ideal indicator of the provenance of BIF deposits (Lan et
420 al. 2019a). However, many BIF-hosted Fe deposits in the NCB have

421 undergone various degrees of metamorphism, recrystallisation, and
422 hydrothermal alteration (Deng et al. 2017; Rasmussen and Muhling 2018; Lan
423 et al. 2019b). It is still unclear whether the original magnetite compositions in
424 BIFs were modified during secondary processes and, if so, to what extent
425 have the compositions been modified (c.f. Lan et al. 2019a, 2019b). In this
426 study, we completed mineralogical and EPMA trace elemental analyses of
427 magnetite from the BIFs and high-grade Fe ores, northeastern NCB. The
428 results were compared with those of unmetamorphosed BIFs worldwide to
429 understand how the original compositions of magnetite in BIFs were modified
430 during different metamorphic grades (Chung et al. 2015). The high-grade
431 metamorphic and modified magnetite in the BIFs and high-grade Fe ores of
432 the eastern NCB is locally fragmented or fractured, embayed, forms mm- to
433 μm-scale bands (Fig. 4c), which is significantly different from the primary, fine-
434 grained, granular magnetite in unmetamorphosed BIFs (Chung et al. 2015).
435 Furthermore, the modified magnetite in the high-grade Fe ores of the eastern
436 NCB has elevated Fe and reduced Al, Ti, K, Mg and Mn compared with that in
437 BIFs (Supplementary Table S1; Fig. 11). Such a change in the magnetite
438 composition is largely controlled by silicate and retrograde greenschist-facies
439 minerals that formed during retrogressive metamorphism with the decreasing
440 temperature (Rasmussen and Muhling 2018). For example, our EPMA trace
441 element map shows that the edges of magnetite grains in the high-grade Fe
442 ore are in contact with retrograde greenschist-facies minerals such as epidote
443 and allanite, and the rims are remarkably enriched in Al, Ti, K, and Mg
444 compared to the cores (Fig. 5). The magnetite in the high-grade Fe ore is also
445 enriched in Fe locally (Fig. 5a). All these features indicate that elemental

446 diffusion and exchange have proceeded between magnetite and retrograde
447 mineral assemblages during high-grade Fe mineralisation and retrogressive
448 metamorphism. These metamorphic events have resulted in the extensive
449 modification of the original compositions of magnetite in BIFs (c.f. Rasmussen
450 and Muhling 2018; Lan et al. 2019a, 2019b). Other examples of the high-
451 grade mineralisation and retrogressive metamorphic magnetite in modified
452 BIF-hosted iron deposits along the southern margin of the NCB have similar
453 characteristics (Lan et al. 2019a, 2019b). These results remind us that it is
454 necessary to calibrate the original experimental data of Al and Ti when
455 determining the metamorphosed magnetite in the BIFs (Fig. 11). The
456 compositions of these elements from magnetite in the BIFs were modified
457 during remobilisation and retrogressive metamorphism.

458 Apatite is relatively stable over a wide variety of geological processes
459 including weathering, transport, and weak hydrothermal alteration (Cook et al.
460 2016; Andersson et al. 2019; Xing et al. 2020; Cao et al. 2021). However, it
461 has also been noted that acids can alter apatite and, as a result, the
462 compositions would be partly or completely modified (Peng et al. 1997; Piccoli
463 and Candela 2002; Andersson et al. 2019; Xing et al. 2020; Gillespie et al.
464 2021). Apatite that has experienced significant hydrothermal alteration might
465 offer insight into the intensity of chemical exchanges during alteration (e.g.,
466 Bouzari et al. 2016; Xing et al. 2020; Yu et al. 2021). In this study, altered
467 zones in apatite are reduced in Ca, P, F, La, Ce, Nd, δCe, δEu, and total
468 REEs contents compared with the non-altered zones in apatite (Figs. 12 and
469 13). The altered zones display sharp compositional boundaries with the non-
470 altered zones (Figs. 6, 7 and 8). They also have pervasive micro-porosities

and fluid inclusions (Fig. 4g–i). Such features are consistent with a fluid-driven, coupled dissolution-reprecipitation process (Harlov et al. 2005; Li and Zhou 2015; Zeng et al. 2016; Azadbakht et al. 2018). During dissolution and reprecipitation, elements can be redistributed from the original apatite to newly crystallised apatite through hydrothermal fluids, and a series of complex chemical exchanges take place between apatite and the reactive fluid (Prowatke and Klemme 2006; Putnis 2009; Andersson et al. 2019). As a result, many trace elements such as Ca, P, F, La, Ce, Nd, and total REEs are leached out from the altered apatite zones (Figs. 12 and 13). This is consistent with the coexistence of apatite and greenschist-facies minerals that formed during retrograde metamorphism (e.g., epidote, allanite and titanite; Figs. 4g–i, 6a, 7a and 8a). Epidote, allanite and titanite can form in retrograde metamorphism when the REEs are released during fluid-driven alteration immediately reprecipitating into new zones (Harlov and Förster 2003; Harlov 2015; Andersson et al. 2019). The different geochemical compositions of the altered and non-altered apatite zones confirm that the Huogezhuang BIF-hosted iron deposit has undergone extensive metasomatism, during which some of the apatite grains have been hydrothermally altered.

Magnetite-apatite assemblage in BIFs and insights into high-grade Fe mineralisation during retrogressive metamorphism

Many authors have discussed source of iron and process of high-grade Fe mineralisation in BIFs based on studies involving trace element and isotope geochemistry, statistics, and thermodynamics (Alibo and Nozaki 1999; Li et al. 2008; Shi et al. 2019a, 2019b; Yang et al. 2019). The common proposed source of iron is from continents, sites of submarine hydrothermal

496 activities, the mixture of seawater and high-temperature hydrothermal fluids,
497 and submarine hydrothermal leaching of the oceanic crust, and most of the
498 magnetite (being the mixed ferrous and ferric Fe_3O_4) is formed by the
499 replacement of siderite ($FeCO_3$) and other Fe-rich minerals after burial (e.g.,
500 Ghosh and Baidya 2017; Haugaard et al. 2017; Rasmussen and Muhling
501 2018; Tong et al. 2021). Two controversial models have been proposed for
502 the process of high-grade Fe mineralisation induced by hydrothermal and
503 metamorphic events: (1) iron is dissolved and migrated by hydrothermal
504 fluids, and then precipitated under favourable conditions (Yang et al. 2019;
505 Zhang et al. 2021); and (2) silica is removed from the BIFs by fluids, and the
506 residual magnetite remains in situ to form high-grade Fe ores (Zhang et al.
507 2014a, 2014b, 2021; Li et al. 2015a). An analogy of the deformation of the
508 BIFs in the NCB may help explain whether what is seen in this area is similar
509 to the BIFs in Western Australia. Egglseder et al. (2017) combined micro-
510 tectonic, field geology and 3D implicit modelling techniques to establish a link
511 between deformation structures at various scales from the BIF-hosted high-
512 grade iron deposits of the Hamersley Province in Australia, and concluded
513 that the deformation not only formed suitable fluid channels, but that folding
514 and shearing also resulted in significant synkinematic removal of gangue
515 minerals. Angerer and Hagemann (2010) proposed that a late-stage brittle
516 segmentation of BIF and reactivation of faults due to deformation of the
517 Koolyanobbing greenstone belt in Western Australia. At the alteration stage,
518 the silicon is leached out from the iron formation, a thin layer of residues of
519 iron oxides and carbonate rocks have been hydrothermally altered (Egglseder
520 et al. 2017). The hydrothermal alteration zones record the transformation of

low-grade BIF to high-grade iron ore (Thorne et al. 2014; Perring et al. 2020). Li et al. (2019, 2020) and Sun et al. (2020) further proposed that faults in the BIFs acted as channels through which silica undersaturated alkaline meteoric fluids moved downward and leached the BIFs during tectonic extension.

Experimental studies by Hou et al. (2018, 2020) on the immiscible hydrous Fe–Ca–P melts provide new evidence for the generation of iron oxide-apatite (IOA) mineralisation. They proposed the possibility that iron-magma was either formed by liquid immiscibility or magnetite-bubble flotation. Crystallizing magnetite and apatite grains are preferentially wetted by immiscible Fe-rich melts, and complete crystallisation of a crystal Fe-rich melt mush leads to the formation of IOA mineralisation (Hou et al. 2018, 2020). The intergrowth of the magnetite-apatite assemblage is widely developed at the Huogezhuang BIF deposit, and may provide new clues to the initial hydrothermal genesis of the BIFs. As the precursor phase to the BIF minerals, ferrihydrite has acted as a carrier of Fe, Si and P elements to the seafloor (Alibert 2016). The material source of magnetite and apatite would be from Fe-rich silicate melts, and then the hydrothermal Fe + Si + P fluids mixed with seawater to crystallize the magnetite and apatite (Figs. 14 and 15a). The systematically analyses show the magnetite and apatite in BIFs are relatively richer in $Na_2O + K_2O$ and Al_2O_3, and poorer in $FeO_T + CaO + P_2O_5$ than those of from the high-grade Fe ores (Supplementary Table S1; Fig. 14). The contents of SiO_2 in magnetite + apatite from BIFs and high-grade Fe ores are almost the same. These geochemical features may indicate remobilisation of Fe and immobility of silicon during the transition from BIFs to high-grade Fe ores. In addition, the magnetite and apatite in BIFs and high-grade Fe ores

546 are overgrown by greenschist-facies minerals formed during retrograde
547 metamorphism (e.g., chlorite, epidote, allanite and titanite; Figs. 4g–i, 5a, 6a,
548 7a and 8a), suggesting that the high-grade Fe mineralisation may be related
549 to retrogressive metamorphism. This is consistent with the later regional
550 metamorphic event (ca. 1950–1850 Ma) in the Miyun Terrane of the eastern
551 NCB. The retrograde metamorphism may induce and drive the remobilisation
552 of iron in BIFs, making it high-grade Fe ores.

553 Therefore, we propose that the high-grade Fe ores represent products
554 after leaching of iron during breakdown of the BIFs, the reprecipitation of iron
555 is mainly responsible for the remobilisation and formation of magnetite during
556 retrogressive metamorphism. Meanwhile, the remnant Na_2O + K_2O + Al_2O_3
557 with the REEs likely formed accessory silicate minerals (such as chlorite,
558 epidote, allanite and titanite) within the BIFs and wall rocks (Fig. 15b).

559 **Implications**

560 The chemical compositions recorded in modified magnetite and
561 hydrothermal apatite from BIFs provide essential insights into the supernormal
562 enrichment of iron during retrogressive metamorphism of BIFs. Compared
563 with low-grade BIFs, the modified magnetite in high-grade Fe ore has an
564 increase in Fe, and decreases in Al, Ti, K, Mg, and Mn, which are controlled
565 by breakdown of BIFs, and silicate and retrograde greenschist-facies minerals
566 formed during retrogressive metamorphism with the decreasing temperature
567 and acids. Retrograde metamorphism drives the remobilisation of iron in BIFs,
568 and the high-grade iron ores are formed by leaching of iron during breakdown
569 of BIFs. Diffusion and exchanges of elements between modified magnetite
570 and retrograde mineral assemblages effectively demonstrate the high-grade

Fe mineralisation during retrogressive metamorphism, during which some of the apatite grains have been hydrothermally altered. REEs are leached out from the hydrothermal apatite and enter the retrograde greenschist-facies minerals during retrogressive metamorphism. Furthermore, *in* situ U–Pb geochronology on apatite intergrown with magnetite has also dated the high-grade BIF-hosted mineralisation. Modified magnetite and hydrothermal apatite in BIFs are ideal indicator minerals to study the enrichment mechanism from low-grade BIFs to high-grade Fe ores during retrograde metamorphism, which enables us to better understand the remobilisation of iron, and metamorphism of iron deposits hosted by BIFs.

Acknowledgements

This study is jointly supported by the National Natural Science Foundation of China (Numbers 92162101, 41872080), the National Key Research and Development Project of China (Number 2020YFA0714802), and the Most Special Fund from the State Key Laboratory of Geological Processes and Mineral Resources in China University of Geosciences, Beijing (CUGB), China (Number MSFGPMR201804). We thank Prof. Kunfeng Qiu (CUGB) and associate Prof. Shengchao Xue (CUGB), and the staff at the Huogezhuang deposit for their supports in the field. This paper benefits greatly from constructive comments of Prof. Zhaochong Zhang and the anonymous reviewers. We are also grateful to the Editor Prof. Hongwu Xu and the Associate Editor Prof. Thomas Mueller for their valuable help in handing this paper.

References cited

Adomako-Ansah, K., Mizuta, T., Ishiyama, D., and Hammond, N.Q. (2017) Nature of ore-forming fluid and formation conditions of BIF-hosted gold mineralization in the Archean Amalia greenstone belt, South Africa: Constraints from fluid inclusion and stable isotope studies. Ore Geology Reviews, 89, 609–626.

Aftabi, A., Atapour, H., Mohseni, S., and Babaki, A. (2021) Geochemical discrimination among different types of banded iron formations (BIFs): A comparative review. Ore Geology Reviews, 136, 104244.

Alibert, C. (2016) Rare earth elements in Hamersley BIF minerals. Geochimica et Cosmochimica Acta, 184, 311–328.

Alibo, D.S., and Nozaki, Y. (1999) Rare earth elements in seawater: Particle association, shale-normalization, and Ce oxidation. Geochimica et Cosmochimica Acta, 63, 363–372.

Andersson, S.S, Wagner, T., Jonsson, E., Fusswinkel, T., and Whitehouse, M.J. (2019) Apatite as a tracer of the source, chemistry and evolution of ore-forming fluids: The case of the Olserum-Djupedal REE-phosphate mineralisation, SE Sweden. Geochimica et Cosmochimica Acta, 255, 163–187.

Angerer, T., and Hagemann, S.G. (2010) The BIF-hosted high-grade iron ore deposits in the Archean Koolyanobbing greenstone belt, western Australia: Structural control on synorogenic- and weathering-related magnetite-, hematite-, and goethite-rich iron ore. Economic Geology, 105, 917–945.

618 Angerer, T., Hagemann, S.G., and Danyushevsky, L. (2013) High-grade iron
619 ore at Windarling, Yilgarn Craton: A product of syn-orogenic deformation,
620 hypogene hydrothermal alteration and supergene modification in an
621 Archean BIF-basalt lithostratigraphy. Mineralium Deposita, 48, 697–728.
622 Angerer, T., Hagemann, S.G., Walde, D.H.G., Halverson, G.P., and Boyce,
623 A.J. (2016) Multiple metal sources in the glaciomarine facies of the
624 Neoproterozoic Jacadigo iron formation in the “Santa Cruz deposit”,
625 Corumbá, Brazil. Precambrian Research, 275, 369–393.
626 Azadbakht, Z., Lentz, D.R., and McFarlane, C.R. (2018) Apatite chemical
627 compositions from Acadian-related granitoids of New Brunswick, Canada:
628 Implications for petrogenesis and metallogenesis. Minerals, 8, 598.
629 Bagas, L., Bierlein, F., Jiang, S.H., Liu, Y.F., and Zhang, L.L. (2020) Review
630 of the regional nomenclature and tectonic setting for Mesozoic gold
631 deposits in the Malanyu Anticline area of Eastern Hebei Province, North
632 China. International Geology Review, 63, 2257–2278.
633 Beijing Bureau of Geology and Mineral resources. (1991) Regional geology of
634 Beijing City. Beijing, Geological Publishing House, p. 461–504 (in
635 Chinese).
636 Bouzari, F., Hart, C.J.R., Bissig, T., and Barker, S. (2016) Hydrothermal
637 alteration revealed by apatite luminescence and chemistry: A potential
638 indicator mineral for exploring covered porphyry copper deposits.
639 Economic Geology, 111, 1397–1410.
640 Cao, M.J., Evans, N.J., Hollings, P., Cooke, D.R., McInnes, B.I.A., and Qin,
641 K.Z. (2021) Apatite texture, composition, and O-Sr-Nd isotope signatures
642 record magmatic and hydrothermal fluid characteristics at the Black

643 Mountain porphyry deposit, Philippines. Economic Geology, 116, 1189–
644 1207.
645 Chen, M.H., Bagas, L., Liao, X., Zhang, Z.Q., and Li, Q.L. (2019)
646 Hydrothermal apatite SIMS Th–Pb dating: Constraints on the timing of
647 low-temperature hydrothermal Au deposits in Nibao, SW China. Lithos,
648 324–325, 418–428.
649 Chung, D., Zhou, M.F., Gao, J.F., and Chen, W.T. (2015) In-situ LA-ICP-MS
650 trace elemental analyses of magnetite: The late Palaeoproterozoic
651 Sokoman Iron Formation in the Labrador Trough, Canada. Ore Geology
652 Reviews, 65, 917–928.
653 Clout, J.M.F., and Simonson, B.M. (2005) Precambrian iron formations and
654 iron formations-hosted ore deposits. Economic Geology 100th
655 Anniversary Volume, 643–679.
656 Cook, N., Ciobanu, C., George, L., and Ehrig, K. (2016) Trace element
657 analysis of minerals in magmatic-hydrothermal ores by laser ablation
658 inductively-coupled plasma mass spectrometry: Approaches and
659 opportunities. Minerals, 6, 1–34.
660 Dai, Y.P., Zhang, L.C., Zhu, M.T., Wang, C.L., Liu, L., and Xiang, P. (2014)
661 The composition and genesis of Mesoarchean Dagushan banded iron
662 formation in the Anshan area, the North China craton. Ore Geology
663 Reviews, 63, 353–373.
664 Dai, Y.P., Zhu, Y.D., Zhang, L.C., and Zhu, M.T. (2017) Meso- and
665 Neoarchean banded iron formations and genesis of high-grade magnetite
666 ores in the Anshan-Benxi area, North China Craton. Economic Geology,
667 112, 1629–1651.

668 Deng, J., Wang, Q.F., and Li, G.J. (2017) Tectonic evolution, superimposed
669 orogeny, and composite metallogenic system in China. Gondwana
670 Research, 50, 216–266.
671 Deng, J., Wang, C.M., Bagas, L., Santosh, M., and Yao, E.Y. (2018) Crustal
672 architecture and metallogenesis in the south-eastern North China Craton.
673 Earth-Science Reviews, 182, 251–272.
674 Diwu, C.R., Sun, Y., Lin, C.L., and Wang, H.L. (2010) LA–(MC)–ICPMS U-Pb
675 zircon geochronology and Lu–Hf isotope compositions of the Taihua
676 Complex on the southern margin of the North China Craton. Chinese
677 Science Bulletin, 55, 2557–2571.
678 Diwu, C.R., Sun, Y., Zhao, Y., and Lai, S.C. (2014) Early Paleoproterozoic
679 (2.45–2.20 Ga) magmatic activity during the period of global magmatic
680 shutdown: Implications for the crustal evolution of the southern North
681 China Craton. Precambrian Research, 255, 627–640.
682 Duan, H.Y., Wang, C.M., Shi, K.X., Wang, C.N., Chen, Q., Zhu, J.X., and
683 Qian, J.L. (2021) Insights into characterization and genesis of the
684 Tieshanmiao banded iron formation deposit, China: Evidence from zircon
685 U–Pb dating and geochemistry. Ore Geology Reviews, 138, 104329.
686 Duuring, P., Hagemann, S.G., Novikova, Y., Cudahy, T., and Laukamp, C.
687 (2012) Targeting iron ore in banded iron formations using ASTER data:
688 Weld Range greenstone belt, Yilgarn Craton, Western Australia.
689 Economic Geology, 107, 585–597.
690 Duuring, P., Hagemann, S.G., Banks, D.A., and Schindler, C. (2018) A
691 synvolcanic origin for magnetite-rich orebodies hosted by BIF in the Weld
692 Range District, Western Australia. Ore Geology Reviews, 93, 211–254.

693 Egglseder, M.S., Cruden, A.R., Dalstra, H.J., and Nicholas, L. (2017) The role
694 of deformation in the formation of banded iron formation-hosted high-
695 grade iron ore deposits, Hamersley Province (Australia). Precambrian
696 Research, 296, 62–77.
697 Fang, T.M., Sun, Y.H., Cheng, X.B., Liu, H., Wu, H.J., and Wei, B. (2017)
698 Geochemical characteristics and metallogenic age of BIF type Fe deposit
699 at Shachang in Miyun County, Beijing. Contributions to Geology and
700 Mineral Resources Research, 32, 42–49 (in Chinese with English
701 abstract).
702 Ghosh, R., and Baidya, T.K. (2017) Mesoarchean BIF and iron ores of the
703 Badampahar greenstone belt, Iron Ore Group, East Indian Shield.
704 Journal of Asian Earth Sciences, 150, 25–44.
705 Gillespie, J., Kinny, P.D., Kirkland, C.L., Martin, L., Nemchin, A.A., Cavosie,
706 A.J., and Hasterok, D. (2021) Isotopic modelling of Archean crustal
707 evolution from comagmatic zircon–apatite pairs. Earth and Planetary
708 Science Letters, 575, 117194.
709 Green, C.J., Seal II, R.R., Piatak, N.M., Cannon, W.F., McAleer, R.J., and
710 Nord, J.A. (2020) Metamorphic amphiboles in the Ironwood Iron-
711 Formation, Gogebic Iron Range, Wisconsin: Implications for potential
712 resource development. American Mineralogist, 105, 1259–1269.
713 Gross, G.A. (1980) A classification of iron formations based on depositional
714 environments. The Canadian Mineralogist, 18, 215–222.
715 Gross, G.A. (1983) Tectonic systems and the deposition of iron-formation.
716 Precambrian Research, 20, 171–187.

717 Hagemann, S.G., Angerer, T., Duuring, P., Rosière, C.A., Figueiredo e Silva,
718 R.C., Lobato, L., Hensler, A.S., and Walde, D.H.G. (2016) BIF-hosted
719 iron mineral system: A review. Ore Geology Reviews, 76, 317–359.
720 Harlov, D.E., and Förster, H.J. (2003) Fluid-induced nucleation of (Y+REE)-
721 phosphate minerals within apatite: Nature and experiment. Part II.
722 Fluorapatite. American Mineralogist, 88, 1209–1229.
723 Harlov, D.E., Wirth, R., and Förster, H. (2005) An experimental study of
724 dissolution reprecipitation in fluorapatite: Fluid infiltration and the
725 formation of monazite. Contributions to Mineralogy and Petrology, 150,
726 268–286.
727 Harlov, D.E. (2015) Apatite: A fingerprint for metasomatic processes.
728 Elements, 11, 171–176.
729 Haugaard, R., Ootes, L., and Konhauser, K. (2017) Neoarchean banded iron
730 formation within a ~2620 Ma turbidite-dominated deep-water basin, Slave
731 craton, NW Canada. Precambrian Research, 292, 130–151.
732 Hou, T., Charlier, B., Namur, O., Schütte, P., Schwarz-Schampera, U., Zhang,
733 Z.C., and Holtz, F. (2017) Experimental study of liquid immiscibility in the
734 Kiruna-type Vergenoeg iron-fluorine deposit, South Africa. Geochimica et
735 Cosmochimica Acta, 203, 303–322.
736 Hou, T., Charlier, B., Holtz, F., Veksler, I., Zhang, Z.C., Thomas, R., and
737 Namur, O. (2018) Immiscible hydrous Fe-Ca-P melt and the origin of iron
738 oxide-apatite ore deposits. Nature Communications, 9, 1–8.
739 Jackson, S.E., Pearson, N.J., Griffin, W.L., and Belousova, E.A. (2004) The
740 application of laser ablation-inductively coupled plasma-mass

741 spectrometry to in situ U-Pb zircon geochronology. Chemical Geology,
742 211, 47–69.
743 James, H.L. (1954) Sedimentary facies of iron-formation. Economic Geology,
744 49, 235–293.
745 Klein, C. (1978) Regional metamorphism of Proterozoic iron-formation,
746 Labrador Trough, Canada. American Mineralogist, 63, 898–912.
747 Klein, C., and Beukes, N.J. (1993) Sedimentology and geochemistry of the
748 glaciogenic late Proterozoic Rapitan iron-formation in Canada. Economic
749 Geology, 88, 542–565.
750 Klein, C. (2005) Some Precambrian banded iron-formations (BIFs) from
751 around the world: Their age, geologic setting, mineralogy,
752 metamorphism, geochemistry, and origin. American Mineralogist, 90,
753 1473–1499.
754 Konhauser, K.O., Pecoits, E., Lalonde, S.V., Papineau, D., Nisbet, E.G.,
755 Barley, M.E., Arndt, N.T., Zahnle, K., and Kamber, B.S. (2009) Oceanic
756 nickel depletion and a methanogen famine before the Great Oxidation
757 Event. Nature, 458, 750–753.
758 Kumar, K.S., Srinivas, K.N.S.S.S., Kumar, V.P., Prasad, P.P., and
759 Seshunarayana, T. (2018) Magnetic mapping of banded iron formation of
760 Sandur schist belt, Dharwar Craton, India. Journal of the Geological
761 Society of India, 91, 174–180.
762 Kusky, T.M., and Li, J.H. (2003) Paleoproterozoic tectonic evolution of the
763 North China Craton. Journal of Asian Earth Sciences, 22, 383–397.

764 Kusky, T.M., Windley, B.F., and Zhai, M.G. (2007) Tectonic evolution of the
765 North China Block: from orogen to craton to orogen. Geological Society,
766 London, Special Publications, 1, 1–34.
767 Kusky, T.M., Polat, A., Windley, B.F., Burke, K.C., Dewey, J.F., Kidd, W.S.F.,
768 Maruyama, S., Wang, J.P., Deng, H., Wang, Z.S., Wang, C., Fu, D., Li,
769 X.W., and Peng, H.T. (2016) Insights into the tectonic evolution of the
770 North China Craton through comparative tectonic analysis: A record of
771 outward growth of Precambrian continents. Earth-Science Reviews, 162,
772 387–432.
773 Lan, C.Y., Yang, A.Y., Wang, C.L., and Zhao, T.P. (2019a) Geochemistry, U-
774 Pb zircon geochronology and Sm-Nd isotopes of the Xincai banded iron
775 formation in the southern margin of the North China Craton: implications
776 on Neoarchean seawater compositions and solute sources. Precambrian
777 Research, 326, 240–257.
778 Lan, C.Y., Yang, A.Y., Wang, C.L., and Zhao, T.P. (2019b) Trace elemental
779 modification in magnetite from high-grade metamorphosed BIFs in the
780 southern North China Craton. Ore Geology Reviews, 112, 103019.
781 Li, H.M., Chen, Y.C., Li, L.X., and Wang, D.H. (2012) Metallogeny of the iron
782 deposits in China. Beijing, Geological Publishing House, p. 1–246 (in
783 Chinese).
784 Li, H.M., and Zhang, Z.H. (2013) The characteristics and research problems
785 of the iron deposit resources in China. Rock and Mineral Analysis, 32,
786 128–130 (in Chinese).

Li, H.M., Zhang, Z.J., Li, L.X., Zhang, Z.C., Chen, J., and Yao, T. (2014) Types and general characteristics of the BIF-related iron deposits in China. Ore Geology Reviews, 57, 264–287.

Li, H.M., Yang, X.Q., Li, L.X., Zhang, Z.C., Liu, M.J., Yao, T., and Chen, J. (2015a) Desilicification and iron activation-reprecipitation in the high-grade magnetite ores in BIFs of the Anshan-Benxi area, China: Evidence from geology, geochemistry and stable isotopic characteristics. Journal of Asian Earth Sciences, 113, 998–1016.

Li, H.M., Li, L.X., Yang, X.Q., and Cheng, Y.B. (2015b) Types and geological characteristics of iron deposits in China. Journal of Asian Earth Sciences, 103, 2–22.

Li, L.X., Li, H.M., Xu, Y.X., Chen, J., Yao, T., Zhang, L.F., Yang, X.Q., and Liu, M.J. (2015) Zircon growth and ages of migmatites in the Algoma-type BIF-hosted iron deposits in Qianxi Group from eastern Hebei Province, China: Timing of BIF deposition and anatexis. Journal of Asian Earth Sciences, 113, 1017–1034.

Li, L.X., Li, H.M., Liu, M.J., Yang, X.Q., and Meng, J. (2016) Timing of deposition and tectonothermal events of banded iron formations in the Anshan-Benxi area, Liaoning Province, China: Evidence from SHRIMP U-Pb zircon geochronology of the wall rocks. Journal of Asian Earth Sciences, 129, 276–293.

Li, L.X., Zi, J.W., Li, H.M., Rasmussen, B., Wilde, S.A., Sheppard, S., Ma, Y.B., Meng, J., and Song, Z. (2019) High-grade magnetite mineralization at 1.86 Ga in Neoarchean manded iron formations, Gongchangling,

China: In situ U-Pb geochronology of metamorphic-hydrothermal zircon and monazite. Economic Geology, 114, 1159–1175.

Li, L.X., Zi, J.W., Meng, J., Li, H.M., Rasmussen, B., Sheppard, S., Wilde, S.A., and Li, Y.H. (2020) Using in situ monazite and xenotime U-Pb geochronology to resolve the fate of the “missing” banded iron formation-hosted high-grade hematite ores of the North China Craton. Economic Geology, 115, 189–204.

Li, X.C., and Zhou, M.F. (2015) Multiple stages of hydrothermal REE remobilization recorded in fluorapatite in the Paleoproterozoic Yinachang Fe-Cu-(REE) deposit, Southwest China. Geochimica et Cosmochimica Acta, 166, 53–73.

Li, Y.H., Hou, K.J., Wan, D.F., Zhang, Z.J., and Yue, G.L. (2010) Formation mechanism of Precambrian banded iron formation and atmosphere and ocean during early stage of the earth. Acta Geologica Sinica, 84, 1359–1373 (in Chinese with English abstract).

Li, Y.H., Zhang, Z.J., Wu, J.S., and Shang, L.P. (2011) Metamorphic chronology of the BIF in Malanzhuang of eastern Hebei Province and its geological implications. Mineral Deposits, 30, 645–653 (in Chinese with English abstract).

Li, Y.H., Hou, K.J., Wan, D.F., and Zhang, Z.J. (2012) A compare geochemistry study for Algoma- and Superior-type banded iron formations. Acta Petrologica Sinica, 28, 3513–3519 (in Chinese with English abstract).

Li, Z.H., Zhu, X.K., and Tang, S.H. (2008) Characters of Fe isotopes and rare earth elements of banded iron formations from Anshan-Benxi area:

836 Implications for Fe source. Acta Petrologica et Mineralogica, 27, 285–290
837 (in Chinese with English abstract).
838 Liu, Y.S., Gao, S., Hu, Z.C., Gao, C.G., Zong, K.Q., and Wang, D.B. (2010)
839 Continental and oceanic crust recycling–induced melt–peridotite
840 interactions in the Trans–North China Orogen: U–Pb dating, Hf isotopes
841 and trace elements in zircon from mantle xenoliths. Journal of Petrology,
842 51, 537–571.
843 McDowell, F.W., McIntosh, W.C., and Farley, K.A. (2005) A precise ^{40}Ar-^{39}Ar
844 reference age for the Durango apatite (U-Th)/He and fission-track dating
845 standard. Chemical Geology, 214, 249–263.
846 Mücke, A., Annor, A., and Neumann, U. (1996) The Algoma-type iron-
847 formations of the Nigerian metavolcano-sedimentary schist belts.
848 Mineralium Deposita, 31, 113–122.
849 Nadoll, P., Mauk, J.L., Hayes, T.S., Koenig, A.E., and Box, S.E. (2012)
850 Geochemistry of magnetite from hydrothermal ore deposits and host
851 rocks of the Mesoproterozoic Belt Supergroup, United States. Economic
852 Geology, 107, 1275–1292.
853 Nadoll, P., Angerer, T., Mauk, J.L., French, D., and Walshe, J. (2014) The
854 chemistry of hydrothermal magnetite: A review. Ore Geology Reviews,
855 61, 1–32.
856 Paton, C., Woodhead, J.D., Hellstrom, J.C., Hergt, J.M., Greig, A., and Maas,
857 R. (2010) Improved laser ablation U-Pb zircon geochronology through
858 robust downhole fractionation correction. Geochemistry Geophysics
859 Geosystems, 11, 1525–2027.

Peng, G.Y., Juhr, J.F., and McGee, J.J. (1997) Factors controlling sulfur concentrations in volcanic apatite. American Mineralogist, 82, 1210–1224.

Perring, C., Crowe, M., and Hronsky, J. (2020) A new fluid-flow model for the genesis of banded iron formation-hosted martite-goethite mineralization, with special reference to the North and South Flank deposits of the Hamersley Province, Western Australia. Economic Geology, 115, 627–659.

Piccoli, P.M., and Candela, P.A. (2002) Apatite in igneous systems. Reviews in Mineralogy and Geochemistry, 48, 255–292.

Pirajno, F., and Yu, H.C. (2021) Cycles of hydrothermal activity, precipitation of chemical sediments, with special reference to Algoma-type BIF. Gondwana Research, 100, 251–260.

Prowatke, S., and Klemme, S. (2006) Trace element partitioning between apatite and silicate melts. Geochimica et Cosmochimica Acta, 70, 4513–4527.

Putnis, A. (2009) Mineral replacement reactions. In E.H., Oelkers, and J., Schott, Eds., Thermodynamics and Kinetics of Water-Rock Interaction, 70, p. 87–124. Reviews in Mineralogy and Geochemistry, Mineralogical Society of America, Chantilly, Virginia.

Rasmussen, B., and Muhling, J.R. (2018) Making magnetite late again: Evidence for widespread magnetite growth by thermal decomposition of siderite in Hamersley banded iron formations. Precambrian Research, 306, 64–93.

884 Santosh, M. (2010) Assembling North China Craton within the Columbia
885 supercontinent: The role of double-sided subduction. Precambrian
886 Research, 178, 149–167.
887 Santosh, M., Liu, D.Y., Shi, Y.R., and Liu, S.J. (2013) Paleoproterozoic
888 accretionary orogenesis in the North China craton: A SHRIMP zircon
889 study. Precambrian Research, 227, 29–54.
890 Santosh, M., Gao, P., Yu, B., Yang, C.X., and Kwon, S. (2020) Neoarchean
891 suprasubduction zone ophiolite discovered from the Miyun Complex:
892 Implications for Archean-Paleoproterozoic Wilson cycle in the North
893 China Craton. Precambrian Research, 342, 105710.
894 Shen, Q.H., Song, H.X., Yang, C.H., and Wan, Y.S. (2011) Petrochemical
895 characteristics and geological significations of banded iron formations in
896 the Wutai Mountain of Shanxi and Qian'an of eastern Hebei. Acta
897 Petrologica et Mineralogica, 30, 161–171 (in Chinese with English
898 abstract).
899 Shen, Q.H., and Song, H.X. (2015) Progress, prospecting and key scientific
900 problems in origin researches of high-grade iron ore of the banded iron
901 formation (BIF) in the North China craton. Acta Petrologica Sinica, 31,
902 2795–2815 (in Chinese with English abstract).
903 Sheppard, S., Krapez, B., Zi, J.W., Rasmussen, B., and Fletcher, I.R. (2017a)
904 SHRIMP U–Pb zircon geochronology establishes that banded iron
905 formations are not chronostratigraphic markers across Archean
906 greenstone belts of the Pilbara Craton. Precambrian Research, 292,
907 290–304.

908 Sheppard, S., Krapez, B., Zi, J.W., Rasmussen, B., and Fletcher, I.R. (2017b)
909 Young ores in old rocks: Proterozoic iron mineralization in Mesoarchaean
910 banded iron formation, northern Pilbara craton, Australia. Ore Geology
911 Reviews, 89, 40–69.
912 Shi, K.X., Wang, C.M., Bagas, L., Du, B., Yang, L.F., and Chen, Q. (2019a)
913 Genesis of the Hanwang Fe deposit in Neoarchean granite-greenstone
914 succession of the eastern North China Craton. Ore Geology Reviews,
915 105, 387–403.
916 Shi, K.X., Wang, C.M., Santosh, M., Du, B., Yang, L.F., and Chen, Q. (2019b)
917 New insights into Neoarchean-Paleoproterozoic crustal evolution in the
918 North China Craton: Evidence from zircon U–Pb geochronology, Lu–Hf
919 isotopes and geochemistry of TTGs and greenstones from the Luxi
920 Terrane. Precambrian Research, 327, 232–254.
921 Shi, Y.R., and Zhao, X.T. (2017) Early Neoarchean magmatic and
922 Paleoproterozoic metamorphic events in the northern North China
923 Craton: SHRIMP zircon dating and Hf isotopes of Archean rocks from the
924 Miyun Area, Beijing. Acta Geologica Sinica (English Edition), 91, 988–
925 1002.
926 Shi, Z.Q., and Shi, Y.R. (2016) SHRIMP U-Pb ages of zircons from banded
927 magnetite quartzite of Shachang Formation in Miyun area of Beijing and
928 their significance. Journal of Earth Sciences and Environment, 38, 547–
929 557 (in Chinese with English abstract).
930 Skublov, S., and Drugova, G. (2003) Patterns of trace-element distribution in
931 calcic amphiboles as a function of metamorphic grade. The Canadian
932 Mineralogist, 41, 383–392.

933 Soares, M.B., Neto, A.V.C., Zeh, A., Cabral, A.R., Pereira, L.F., Prado,
934 M.G.B., Almeida, A.M.D., Manduca, L.G., Silva, P.H.M., Mabub, R.O.D.,
935 and Schlichta, T.M. (2017) Geology of the Pitangui greenstone belt,
936 Minas Gerais, Brazil: Stratigraphy, geochronology and BIF geochemistry.
937 Precambrian Research, 291, 17–41.
938 Sun, S.S., and McDonough, W.F. (1989) Chemical and isotopic systematics
939 of oceanic basalts: Implications for mantle composition and processes.
940 Geological Society, London, Special Publications, 42, 313–345.
941 Sun, X.H., Tang, H.S., Luan, Y., and Chen, J.H. (2020) Geochronological
942 constraints on the genesis of high-grade iron ore in the Gongchangling
943 BIFs from the Anshan-Benxi area, North China Craton. Ore Geology
944 Reviews, 122, 103504.
945 Tang, L., and Santosh, M. (2018) Neoarchean-Paleoproterozoic terrane
946 assembly and Wilson cycle in the North China Craton: An overview from
947 the central segment of the Trans-North China Orogen. Earth-Science
948 Reviews, 182, 1–27.
949 Tang, L., Santosh, M., and Tsunogae, T. (2019) Petrology, phase equilibria
950 modelling and zircon U-Pb geochronology of garnet-bearing charnockites
951 from the Miyun area: Implications for microblock amalgamation of the
952 North China Craton. Lithos, 324–325, 234–245.
953 Thompson, J., Meffre, S., and Danyushevsky, L. (2018) Impact of air, laser
954 pulse width and fluence on U-Pb dating of zircons by LA-ICP-MS. Journal
955 of Analytical Atomic Spectrometry, 33, 221–230.
956 Thorne, W.S., Hagemann, S.G., Sepe, D., Dalstra, H.J., and Banks, D.A.
957 (2014) Structural control, hydrothermal alteration zonation, and fluid

chemistry of the concealed, high-grade 4EE iron orebody at the Paraburdoo 4E deposit, Hamersley Province, Western Australia. Economic Geology, 109, 1529–1562.

Tong, X.X., Wang, C.L., Peng, Z.D., Li, Y.H., Hao, W.D., Mänd, K., Robbins, L.J., Zhang, L.C., Ke, Q., Zhai, M.G., and Konhauserand, K.O. (2021) Depositional and environmental constraints on the late Neoarchean Dagushan deposit (Anshan-Benxi area, North China Craton): An Algoma-type banded iron formation. Economic Geology, 116, 1575–1597.

Urban, H., Stribrny, B., and Lippolt, H.J. (1992) Iron and manganese deposits of the Urucum District, Mato Grosso do Sul, Brazil. Economic Geology, 87, 1375–1392.

Wan, Y.S., Dong, C.Y., Xie, H.Q., Wang, S.J., Song, M.C., Xu, Z.Y., Wang, S.Y., Zhou, H.Y., Ma, M.Z., and Liu, D.Y. (2012) Formation age of Early Precambrian BIFs in the North China Craton: SHRIMP zircon U–Pb dating. Acta Geologica Sinica, 86, 1447–1478 (in Chinese with English abstract).

Wan, Y.S., Dong, C.Y., Xie, H.Q., Xie, S.W., Liu, S.J., Bai, W.Q., Ma, M.Z., and Liu, D.Y. (2018) Formation age of BIF-bearing Anshan Group supracrustal rocks in Anshan-Benxi Area: New evidence from SHRIMP U–Pb zircon dating. Earth Science, 43, 57–81 (in Chinese with English abstract).

Wang, C.L., Zhang, L.C., Lan, C.Y., and Dai, Y.P. (2014) Petrology and geochemistry of the Wangjiazhuang banded iron formation and associated supracrustal rocks from the Wutai greenstone belt in the North

982 China Craton: Implications for their origin and tectonic setting.
983 Precambrian Research, 255, 603–626.
984 Wang, C.L., Konhauser, K.O., and Zhang, L.C. (2015) Depositional
985 environment of the Paleoproterozoic Yuanjiacun banded iron formation in
986 Shanxi Province, China. Economic Geology, 110, 1515–1539.
987 Wang, C.M., Deng, J., Santosh, M., Carranza, E.J.M., Gong, Q.J., Guo, C.Y.,
988 Xia, R., and Lai, X.R. (2015) Timing, tectonic implications and genesis of
989 gold mineralization in the Xincheng gold deposit, China: C–H–O isotopes,
990 pyrite Rb–Sr and zircon fission track thermochronometry. Ore Geology
991 Reviews, 65, 659–673.
992 Wang, C.M., Lu, Y.J., He, X.Y., Wang, Q.H., and Zhang, J. (2016) The
993 Paleoproterozoic diorite dykes in the southern margin of the North China
994 Craton: Insight into rift-related magmatism. Precambrian Research, 277,
995 26–46.
996 Wang, C.M., Bagas, L., Deng, J., and Dong, M.M. (2018) Crustal architecture
997 and its controls on mineralisation in the North China Craton. Ore Geology
998 Reviews, 98, 109–125.
999 Wiedenbeck, M., Hanchar, J.M., Peck, W.H., Sylvester, P., Valley, J.,
1000 Whitehouse, M., Kronz, A., Morishita, Y., Nasdala, L., and Fiebig, J.
1001 (2004) Further characterisation of the 91500 zircon crystal. Geostandards
1002 and Geoanalytical Research, 28, 9–39.
1003 Wudarska, A., Wiedenbeck, M., Słaby, E., Lepland, A., Birski, Ł., and Simon,
1004 K. (2020) Halogen chemistry and hydrogen isotopes of apatite from the >
1005 3.7 Ga Isua supracrustal belt, SW Greenland. Precambrian Research,
1006 310, 153–164.

1007 Xing, K., Shu, Q.H., Lentz, D.R., and Wang, F.Y. (2020) Zircon and apatite
1008 geochemical constraints on the formation of the Huojihe porphyry Mo
1009 deposit in the Lesser Xing'an Range, NE China. American Mineralogist,
1010 105, 382–396.
1011 Yang, X.Q., Mao, J.W., Jiang, Z.S., Santosh, M., Zhang, Z.H., Duan, S.G.,
1012 and Wang, D.C. (2019) The carboniferous Shikebutai iron deposit in
1013 western Tianshan, northwestern China: Petrology, Fe-O-C-Si isotopes,
1014 and implications for iron pathways. Economic Geology, 114, 1207–1222.
1015 Yu, H.C., Qiu, K.F., Hetherington, C.J., Chew, D., Huang, Y.Q., He, D.Y.,
1016 Geng, J.Z., and Xian, H.Y. (2021) Apatite as an alternative
1017 petrochronometer to trace the evolution of magmatic systems containing
1018 metamict zircon. Contributions to Mineralogy and Petrology, 176, 68.
1019 Zeng, L.P., Zhao, X.F., Li, X.C., Hu, H., and McFarlane, C. (2016) In situ
1020 elemental and isotopic analysis of fluorapatite from the Taocun
1021 magnetite-apatite deposit, Eastern China: Constraints on fluid
1022 metasomatism. American Mineralogist, 101, 2468–2483.
1023 Zhai, M.G., Guo, J.H., and Liu, W.J. (2005) Neoarchean to Paleoproterozoic
1024 continental evolution and tectonic history of the North China Craton: A
1025 review. Journal of Asian Earth Sciences, 24, 547–561.
1026 Zhai, M.G., and Santosh, M. (2011) The early Precambrian odyssey of the
1027 North China Craton: A synoptic overview. Gondwana Research, 20, 6–
1028 25.
1029 Zhai, M.G., Hu, B., Zhao, T.P., Peng, P., and Meng, Q.R. (2015) Late
1030 Paleoproterozoic-Neoproterozoic multi-rifting events in the North China

Craton and their geological significance: A study advance and review. Tectonophysics, 662, 153–166.

Zhai, M.G., Zhu, X.Y., Zhou, Y.Y., Zhao, L., and Zhou, L.G. (2020) Continental crustal evolution and synchronous metallogeny through time in the North China Craton. Journal of Asian Earth Sciences, 194, 104169.

Zhang, L.C., Zhai, M.G., Wan, Y.S., Guo, J.H., Dai, Y.P., Wang, C.L., and Liu, L. (2012) Study of the Precambrian BIF-iron deposits in the North China Craton: Progresses and questions. Acta Petrologica Sinica, 28, 3431–3445 (in Chinese with English abstract).

Zhang, X.J., Zhang, L.C., Xiang, P., Wan, B., and Pirajno, F. (2011) Zircon U–Pb age, Hf isotopes and geochemistry of Shuichang Algoma-type banded iron-formation, North China Craton: Constraints on the ore forming age and tectonic setting. Gondwana Research, 20, 137–148.

Zhang, Z.C., Hou, T., Santosh, M., Li, H.M., Li, J.W., Zhang, Z.H., Song, X.Y., and Wang, M. (2014a) Spatio-temporal distribution and tectonic setings of the major iron deposits in China: An overview. Ore Geology Reviews, 57, 247–263.

Zhang, Z.C., Hou, T., Li, H.M., Li, J.W., Zhang, Z.H., and Song, X.Y. (2014b) Enrichment mechanism of iron in magmatic-hydrothermal system. Acta Petrologica Sinica, 30, 1189–1204 (in Chinese with English abstract).

Zhang, Z.C., Li, H.M., Li, J.W., Song, X.Y., Hu, H., Li, L.X., Chai, F.M., Hou, T., and Xu, D.R. (2021) Geological settings and metallogenesis of high-grade iron deposits in China. Science China Earth Sciences, 64, 691–715.

Zhao, G.C., Wilde, S.A., Cawood, P.A., and Sun, M. (2001) Archean blocks and their boundaries in the North China Craton: lithological, geochemical, structure and P-T path constraints and tectonic evolution. Precambrian Research, 107, 45–73.

Zhao, G.C. (2007) When did plate tectonics begin on the North China Craton? Insights from metamorphism. Earth Science Frontiers, 14, 19–32.

Zhao, G.C., and Zhai, M.G. (2013) Lithotectonic elements of Precambrian basement in the North China Craton: Review and tectonic implications. Gondwana Research, 23, 1207–1240.

Zi, J.W., Rasmussen, R., Muhling, J.R., Fletcher, I.R., Thorne, A.M., Johnsonm, S.P., Cutten, H.N., Dunkley, D.J., and Korhonen, F.J. (2015) In situ U–Pb geochronology of xenotime and monazite from the Abra polymetallic deposit in the Capricorn Orogen, Australia: Dating hydrothermal mineralization and fluid flow in a long-lived crustal structure. Precambrian Research, 260, 91–112.

Zi, J.W., Rasmussen, R., Muhling, J.R., and Fletcher, I.R. (2018) U-Pb geochronology of monazite in Precambrian tuffs reveals depositional and metamorphic histories. Precambrian Research, 313, 109–118.

Figure captions

Figure 1. (a) Geological and tectonic framework showing the BIF-hosted Fe deposits in the North China Block (modified after Zhao et al. 2001; Zhao 2007; Zhang et al. 2012; Wang et al. 2018; Deng et al. 2018, 2020). Abbreviations of complexes: AS = Anshan; CD = Chengde; DF = Dengfeng; EH = Eastern Hebei; ES = Eastern Shandong; FP = Fuping; GY = Guyang; HA = Huai'an; HL = Helanshan; HS = Hengshan; JN = Jining; JP = Jianping; LL = Lvliang; MY = Miyun; NH = Northern Hebei; NL = Northern Liaoning; QL = Qianlishan; SJ = Southern Jilin; SL = Southern Liaoning; TH = Taihua; WD = Wulashan–Daqingshan; WL = Western Liaoning; WS = Western Shandong; WY = Wuyang; WT = Wutai; XH = Xuanhua; ZH = Zanhuang; ZT = Zhongtiao. Abbreviations of blocks: ALS = Alashan; JL = Jiaoliao; JN = Jining; OR = Ordos; QH = Qianhuai; XC = Xuchang; XH = Xuhuai. (b) Geological map of the Miyun area (modified after Beijing Bureau of Geology and Mineral resources 1991).

Figure 2. Geological map (a) and section (b) of the Huogezhuang Fe deposit (modified after Beijing Bureau of Geology and Mineral resources 1991).

Figure 3. Geological sections, field photographs and hand specimens of the ore samples and wall rock from the Huogezhuang BIF-hosted Fe deposit. (a-b) Geological sections showing the ore body with porphyritic granite, chlorite-alteration, and faults. (c) Garnet and calcite distributed in the contact of ore body and garnet gneiss. (d) Calcite vein from the high-grade Fe ore with chlorite-alteration. (e) BIF. (f) High-grade Fe ore.

Figure 4. Representative microphotographs under cross-polarized light and backscattered electron images of the ore samples from the Huogezhuang

BIF-hosted Fe deposit. (a) Magnetite-rich and quartz layers with granulite- to amphibolite-facies (clinopyroxene and hornblende) and greenschist-facies minerals (chlorite and epidote). (b) Magnetite, quartz, apatite, and epidote. (c) Magnetite showing destruction texture. (d-e) Magnetite and coexisting apatite. (f-i) Apatite showing partly altered zones with greenschist-facies minerals (epidote, allanite and titanite). Mineral abbreviations: Mt = magnetite; Ap = apatite; Qtz = quartz; Cpx = clinopyroxene; Hbl = hornblende; Pl = plagioclase; Chl = chlorite; Ep = epidote; Aln = allanite; Ttn = titanite.

Figure 5. Backscattered electron images (a-b) and distributions of selected elements (c-j) in the magnetite grain from the high-grade Fe ore. Mineral abbreviations: Mt = magnetite; Ap = apatite; Qtz = quartz; Ep = epidote.

Figure 6. Backscattered electron images (a), CL images (b) and distributions of selected elements (c-i) in the apatite grain from the high-grade Fe ore. Mineral abbreviations: Mt = magnetite; Ap = apatite; Ep = epidote; Aln = allanite.

Figure 7. Backscattered electron images (a), CL images (b) and distributions of selected elements (c-i) in the apatite grain from the BIF. Mineral abbreviations: Mt = magnetite; Ap = apatite; Ep = epidote; Ttn = titanite.

Figure 8. Backscattered electron images (a), CL images (b) and distributions of selected elements (c-i) in the apatite grain from the BIF. Mineral abbreviations: Mt = magnetite; Ap = apatite; Ep = epidote; Ttn = titanite.

Figure 9. Representative backscattered electron images and U–Pb concordia plots for apatite *in situ* from the Huogezhuang BIF-hosted Fe deposit. (a) High-grade Fe ore (Sample D01DB6). (b) BIF (Sample D01DB5).

Figure 10. Geochronology of high-grade Fe ore and BIF from the Huogezhuang BIF-hosted Fe deposit showing: (a) U–Pb concordia plot for high-grade Fe ore (Sample D01B3) and representative CL images of zircons; (b) U–Pb concordia plot for BIF (Sample D01B5) and representative CL images of zircons; and (c) combined probability density plot for samples D01B3 and D01B5.

Figure 11. (a) Normalised multi-elemental patterns of magnetite from the Huogezhuang BIFs. Normalization values are the average composition of magnetite from the unmetamorphosed BIF in the Sokoman Iron Formation (Chung et al. 2015; Ti = 31 ppm, Al = 128 ppm, Mn = 291 ppm, Mg = 153 ppm, Ca = 84 ppm, V = 23 ppm, Cr = 6 ppm, Co = 14 ppm, Cu = 1 ppm, Zn = 10 ppm). (b) Ti/100–Al/30–Mg + Mn diagram (after Nadoll et al. 2012, 2014). (c-d) Ti/100 + V/10 vs. Al/30 + Mn diagrams (after Nadoll et al. 2012, 2014).

Figure 12. (a) Chondrite-normalised REE patterns of the apatite in the Huogezhuang BIF-hosted Fe deposit. Chondrite normalization values are after Sun and McDonough 1989. (b) Total REE contents in altered and unaltered zones of the apatite. (c) δCe and δEu values in altered and unaltered zones of the apatite. (d) Concentrations of selected elements in altered and unaltered zones of the apatite.

Figure 13. Concentrations of selected elements in altered and unaltered zones of the apatite in the Huogezhuang BIF-hosted Fe deposit.

Figure 14. Geochemical diagrams. (a) TiO_2 + FeO_T + MnO + MgO + CaO + P_2O_5–Na_2O + K_2O + Al_2O_3–SiO_2 diagram (after Hou et al. 2017, 2018). (b) Al_2O_3 vs. Na_2O + K_2O diagram (after Hou et al. 2017, 2018).

1146 **Figure 15.** Schematic model for BIF-hosted high-grade magnetite
1147 mineralisation and modification of the Huogezhuang Fe deposit (after Shi et
1148 al. 2019a; Li et al. 2019). (a) BIF deposition. (b) BIF deposition at ca. 2500-
1149 1900 Ma, and high-grade magnetite mineralisation during retrogressive
1150 metamorphism, modification, and alteration of BIFs at < 1900 Ma.

Supplementary table captions

Supplementary Table S1. Mineral chemical concentrations under electron probe micro-analysis of the magnetite and apatite from the BIF and high-grade Fe ore.

Supplementary Table S2. LA–ICP–MS trace elemental analysis of the apatite *in situ*.

Supplementary Table S3. LA–ICP–MS apatite *in situ* U–Pb dating results.

Supplementary Table S4. LA–ICP–MS zircon U–Pb dating results from the BIF and high-grade Fe ore.

This is the peer-reviewed, final accepted version for American Mineralogist, published by the Mineralogical Society of America.
The published version is subject to change. Cite as Authors (Year) Title. American Mineralogist, in press.
DOI: https://doi.org/10.2138/am-2022-8525. http://www.minsocam.org/

Figure 1

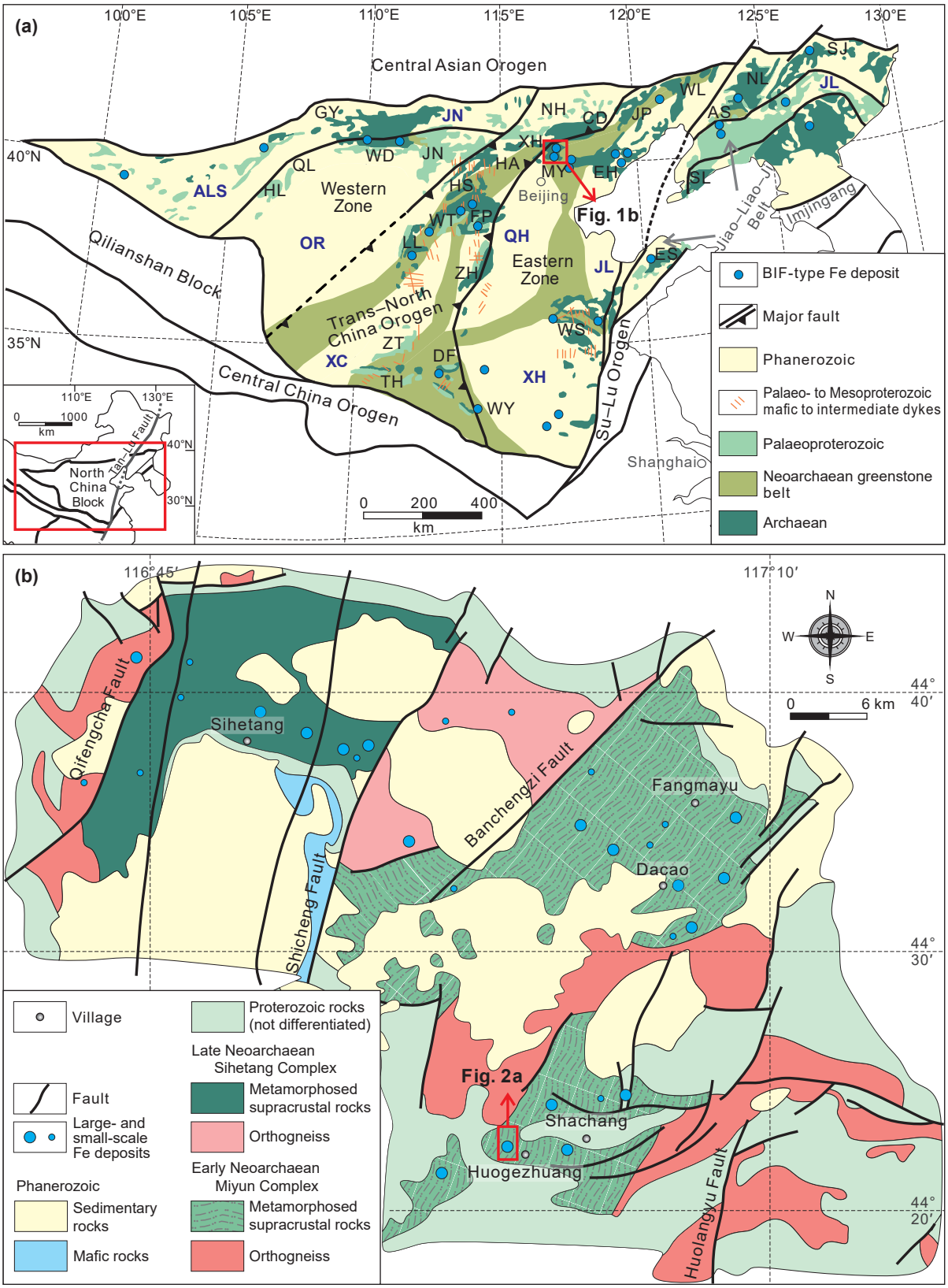

Figure 2

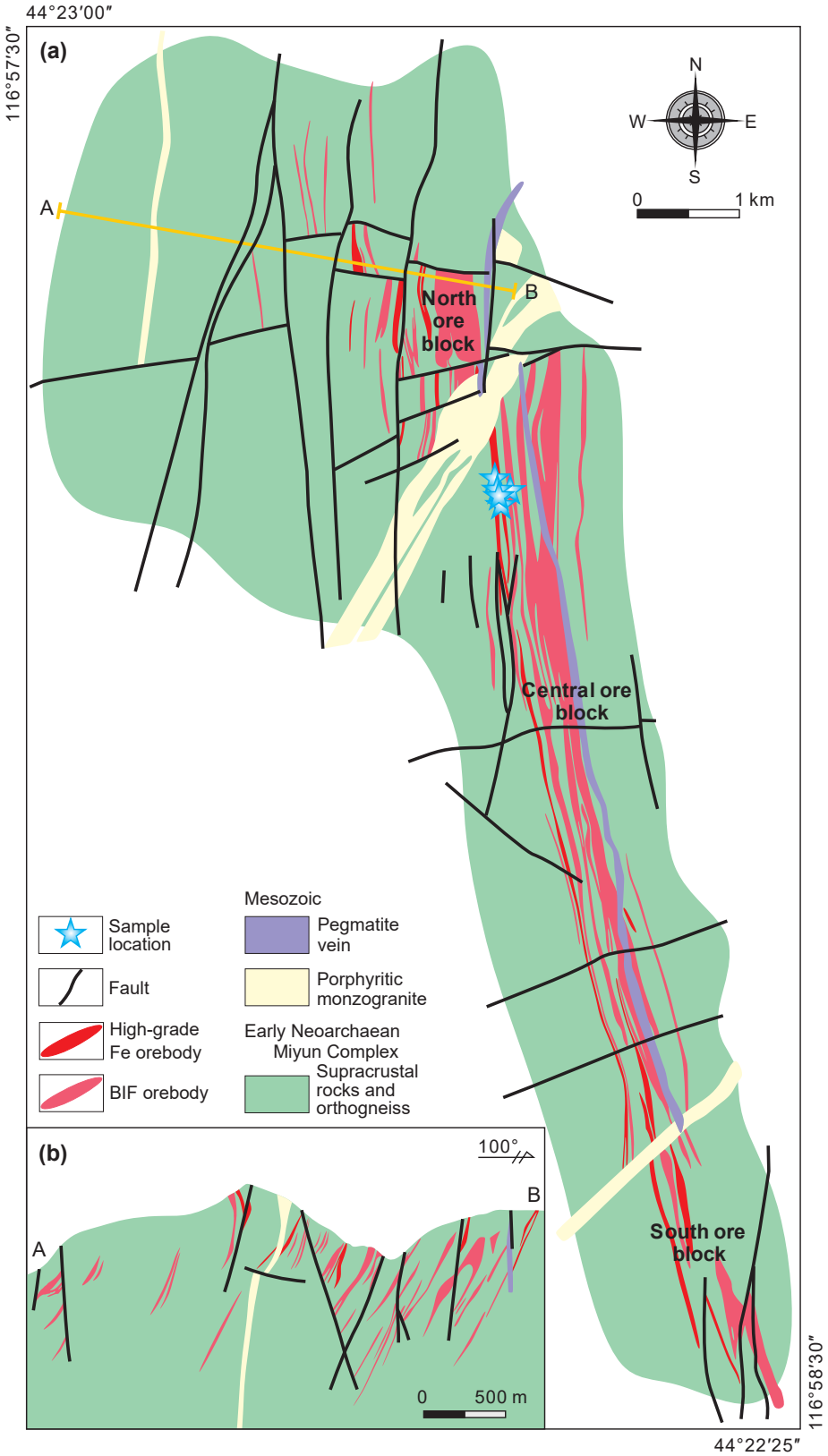

Figure 3

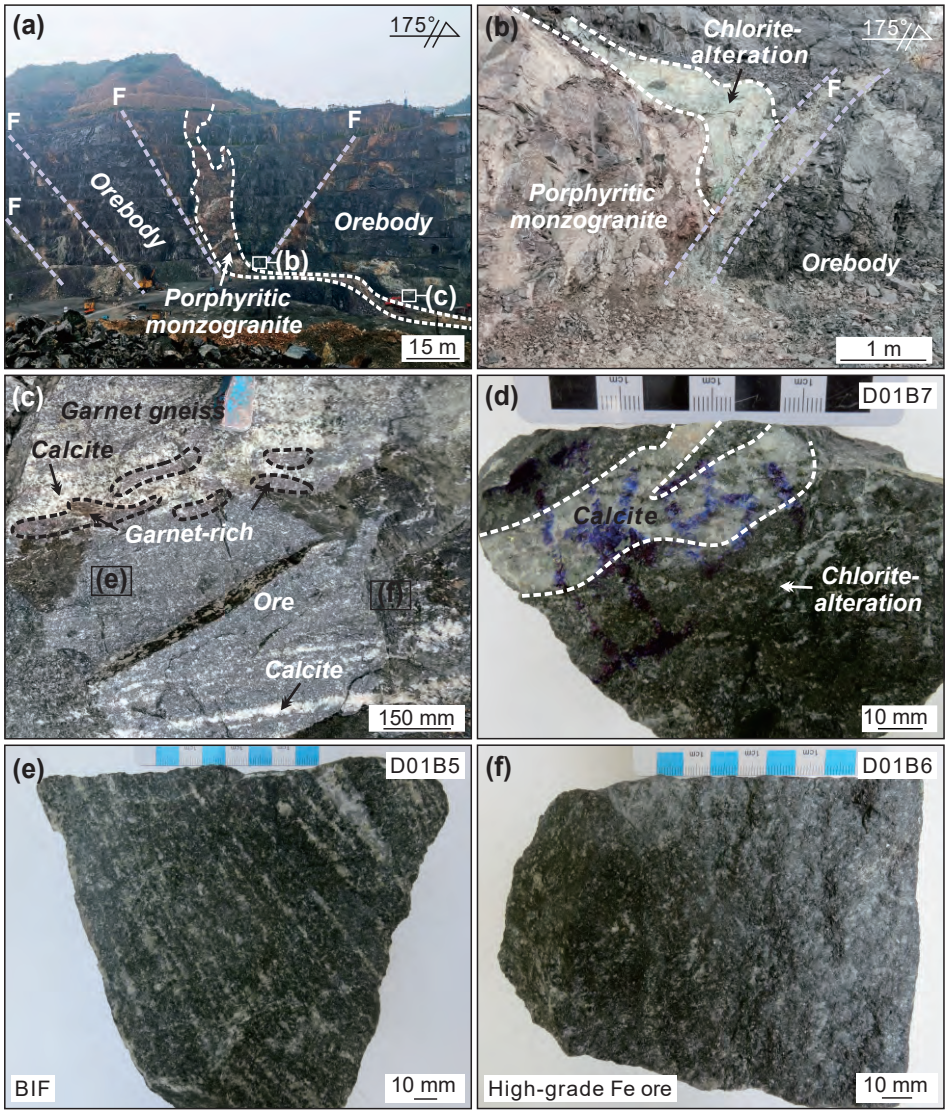

Figure 4

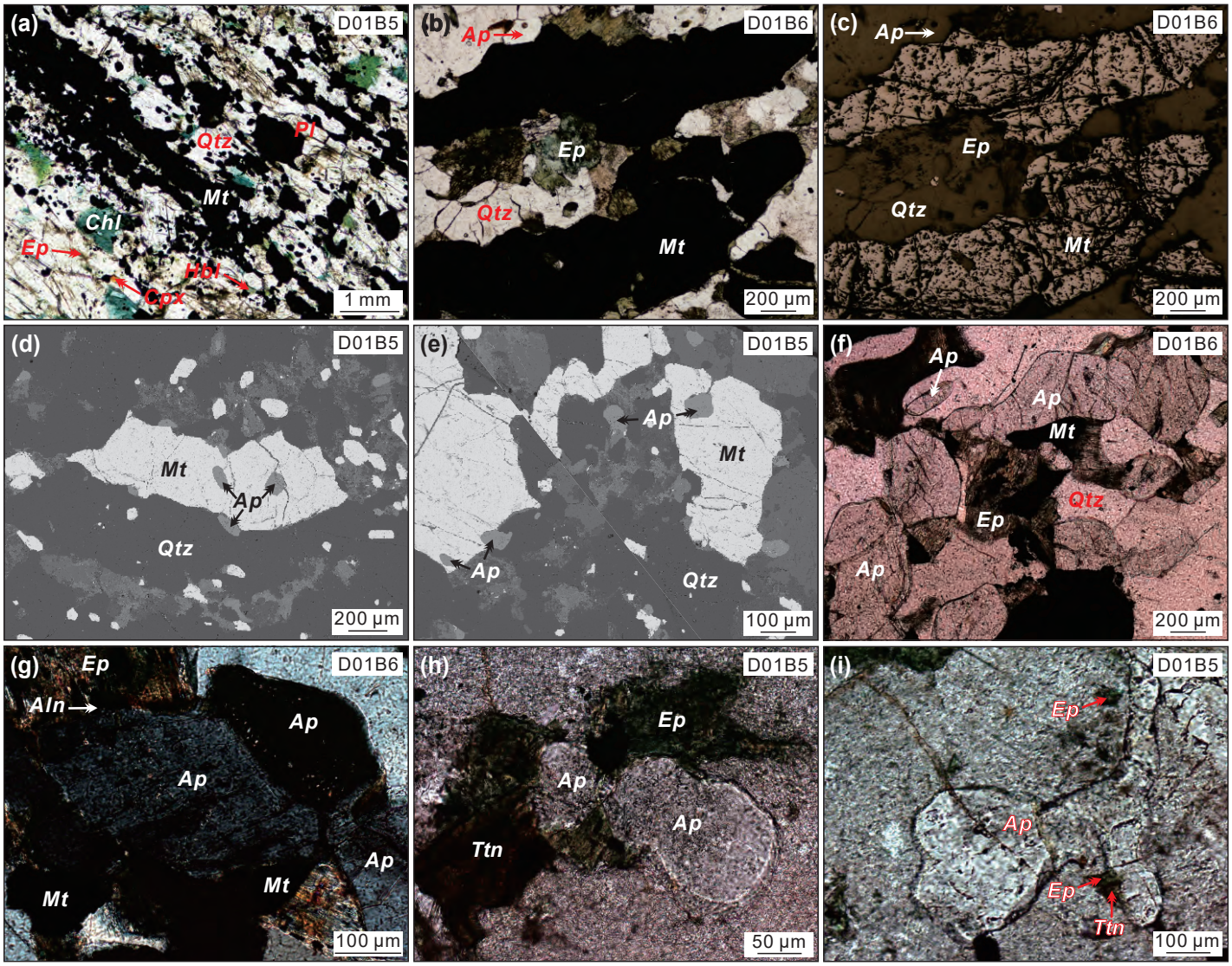

This is the peer-reviewed, final accepted version for American Mineralogist, published by the Mineralogical Society of America.
The published version is subject to change. Cite as Authors (Year) Title. American Mineralogist, in press.
DOI: https://doi.org/10.2138/am-2022-8525. http://www.minsocam.org/

Figure 5

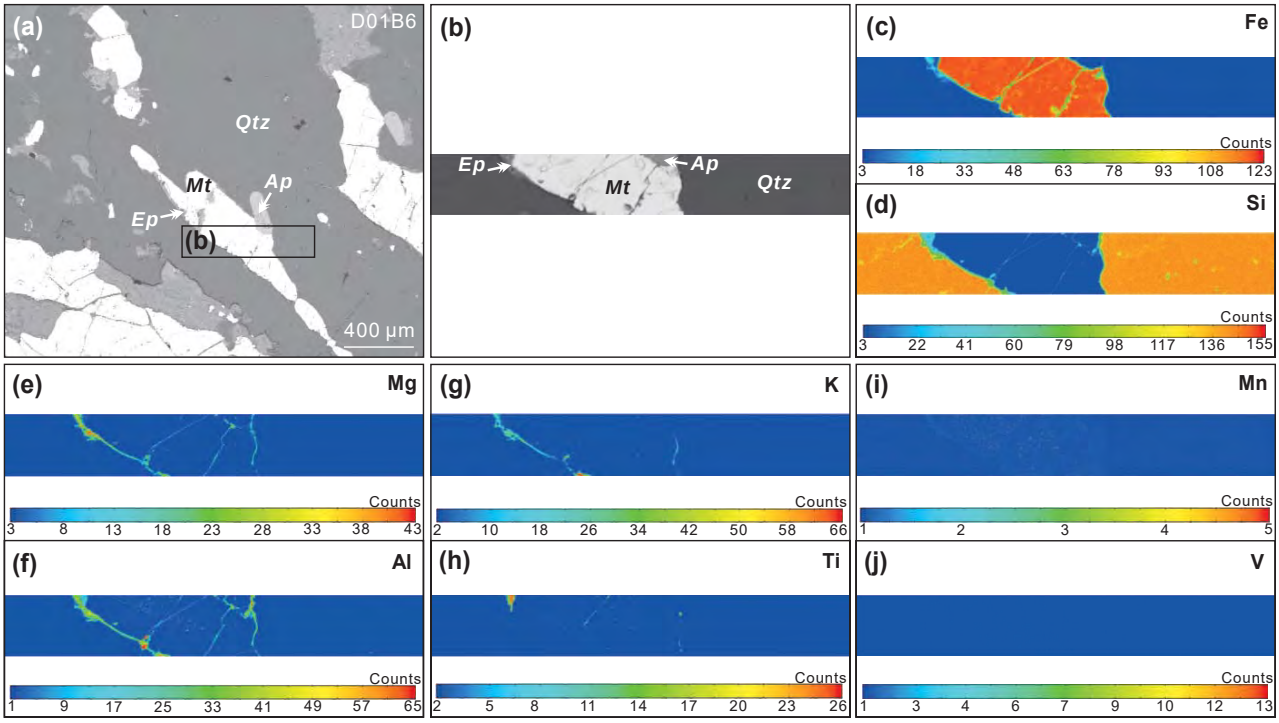

This is the peer-reviewed, final accepted version for American Mineralogist, published by the Mineralogical Society of America.
The published version is subject to change. Cite as Authors (Year) Title. American Mineralogist, in press.
DOI: https://doi.org/10.2138/am-2022-8525. http://www.minsocam.org/

Figure 6

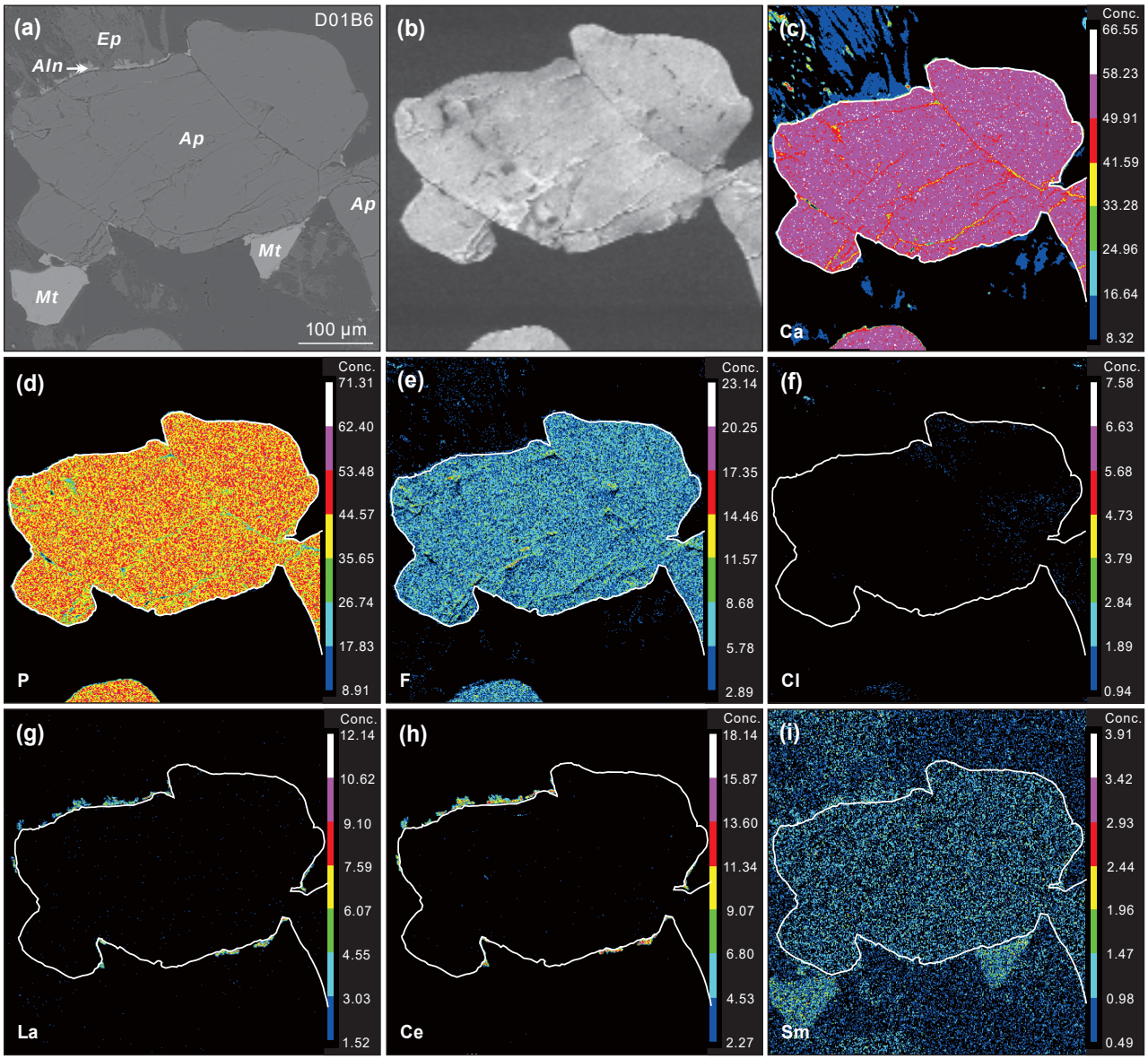

This is the peer-reviewed, final accepted version for American Mineralogist, published by the Mineralogical Society of America.
The published version is subject to change. Cite as Authors (Year) Title. American Mineralogist, in press.
DOI: https://doi.org/10.2138/am-2022-8525. http://www.minsocam.org/

Figure 7

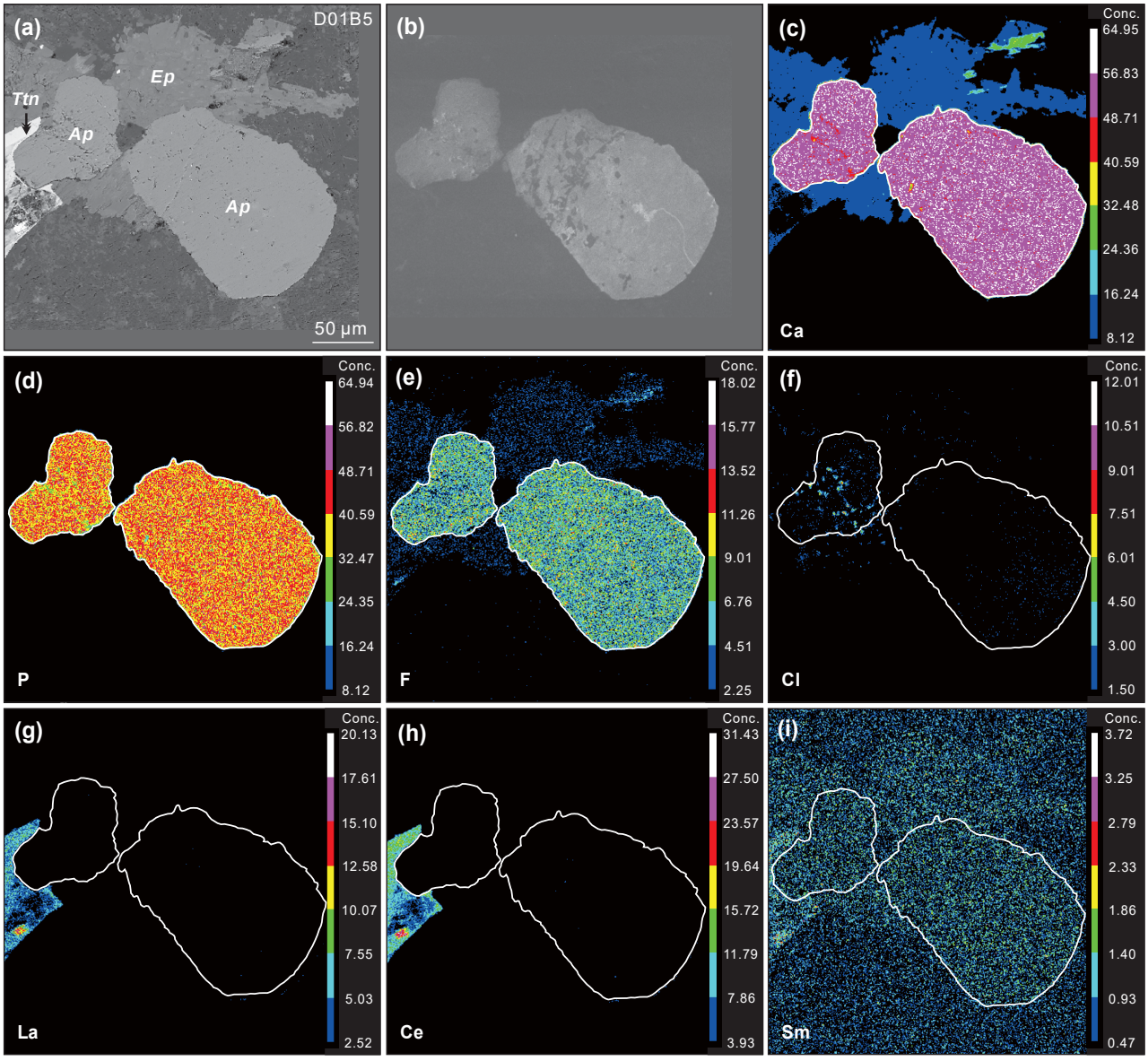

This is the peer-reviewed, final accepted version for American Mineralogist, published by the Mineralogical Society of America.
The published version is subject to change. Cite as Authors (Year) Title. American Mineralogist, in press.
DOI: https://doi.org/10.2138/am-2022-8525. http://www.minsocam.org/

Figure 8

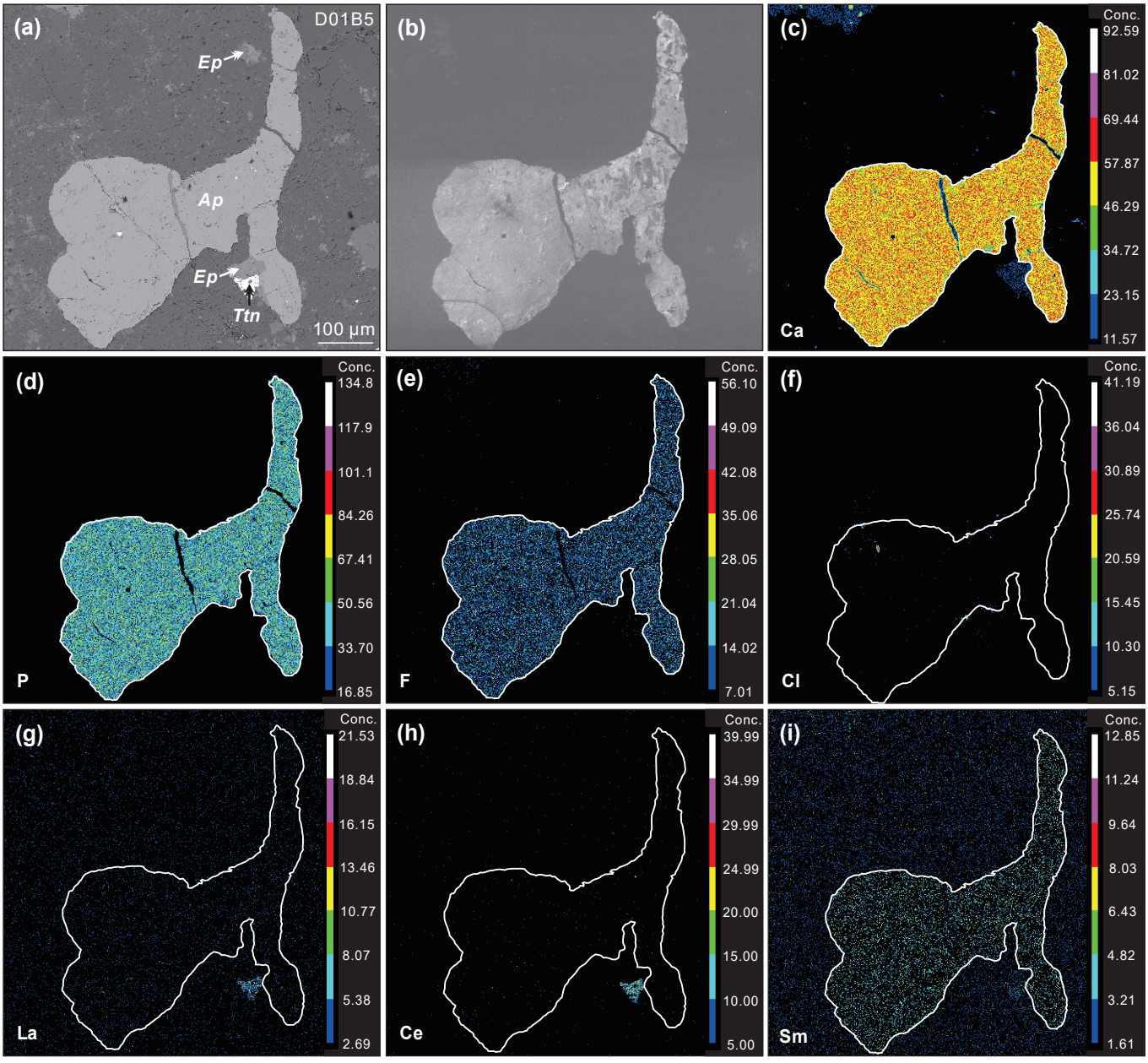

This is the peer-reviewed, final accepted version for American Mineralogist, published by the Mineralogical Society of America.
The published version is subject to change. Cite as Authors (Year) Title. American Mineralogist, in press.
DOI: https://doi.org/10.2138/am-2022-8525. http://www.minsocam.org/

Figure 9

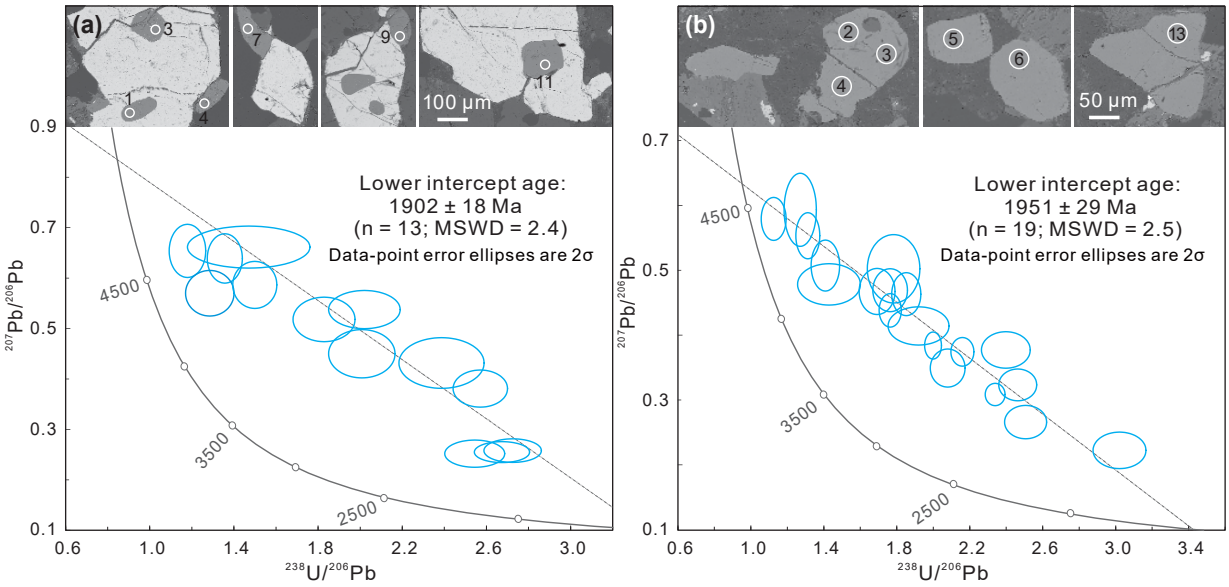

This is the peer-reviewed, final accepted version for American Mineralogist, published by the Mineralogical Society of America.
The published version is subject to change. Cite as Authors (Year) Title. American Mineralogist, in press.
DOI: https://doi.org/10.2138/am-2022-8525. http://www.minsocam.org/

Figure 10

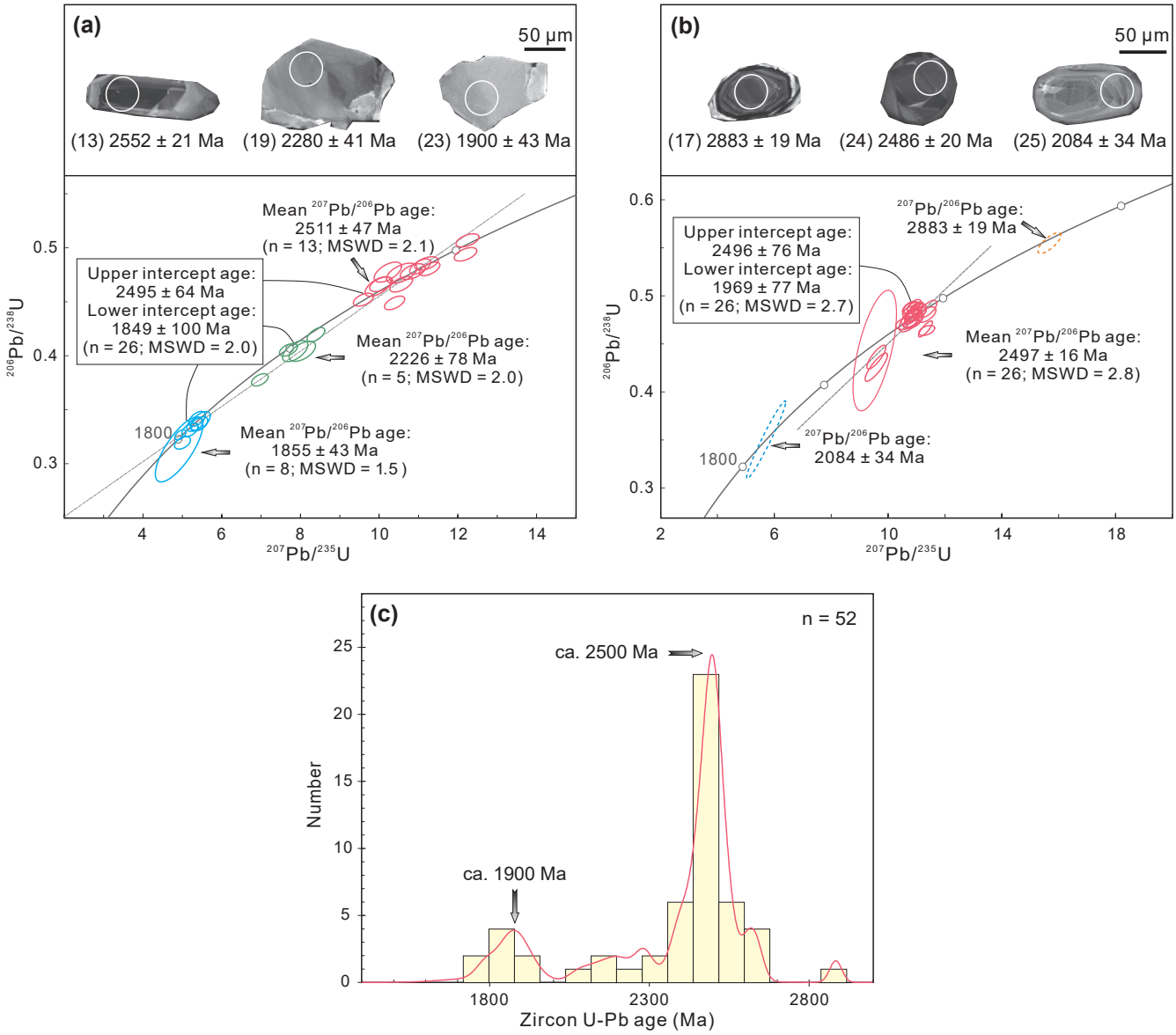

This is the peer-reviewed, final accepted version for American Mineralogist, published by the Mineralogical Society of America.
The published version is subject to change. Cite as Authors (Year) Title. American Mineralogist, in press.
DOI: https://doi.org/10.2138/am-2022-8525. http://www.minsocam.org/

Figure 11

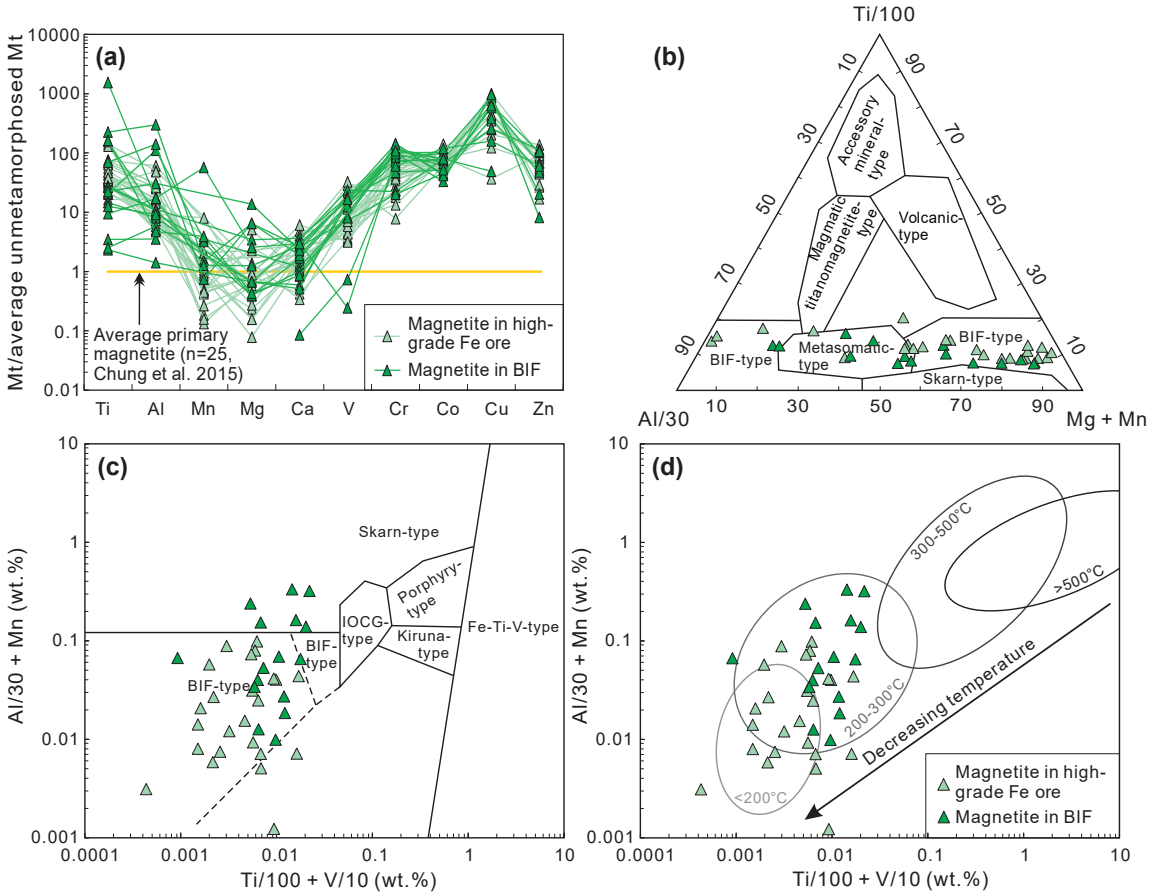

This is the peer-reviewed, final accepted version for American Mineralogist, published by the Mineralogical Society of America.
The published version is subject to change. Cite as Authors (Year) Title. American Mineralogist, in press.
DOI: https://doi.org/10.2138/am-2022-8525. http://www.minsocam.org/

Figure 12

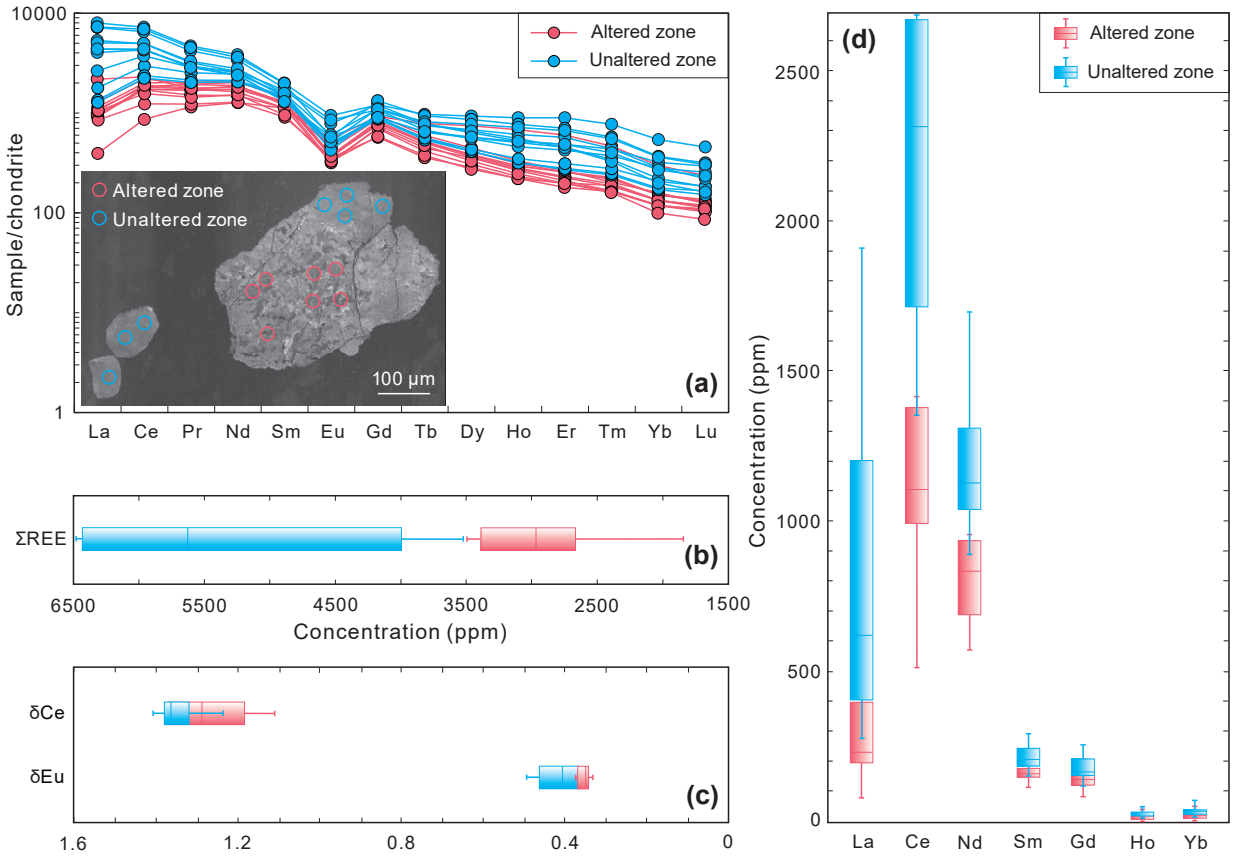

This is the peer-reviewed, final accepted version for American Mineralogist, published by the Mineralogical Society of America.
The published version is subject to change. Cite as Authors (Year) Title. American Mineralogist, in press.
DOI: https://doi.org/10.2138/am-2022-8525. http://www.minsocam.org/

Figure 13

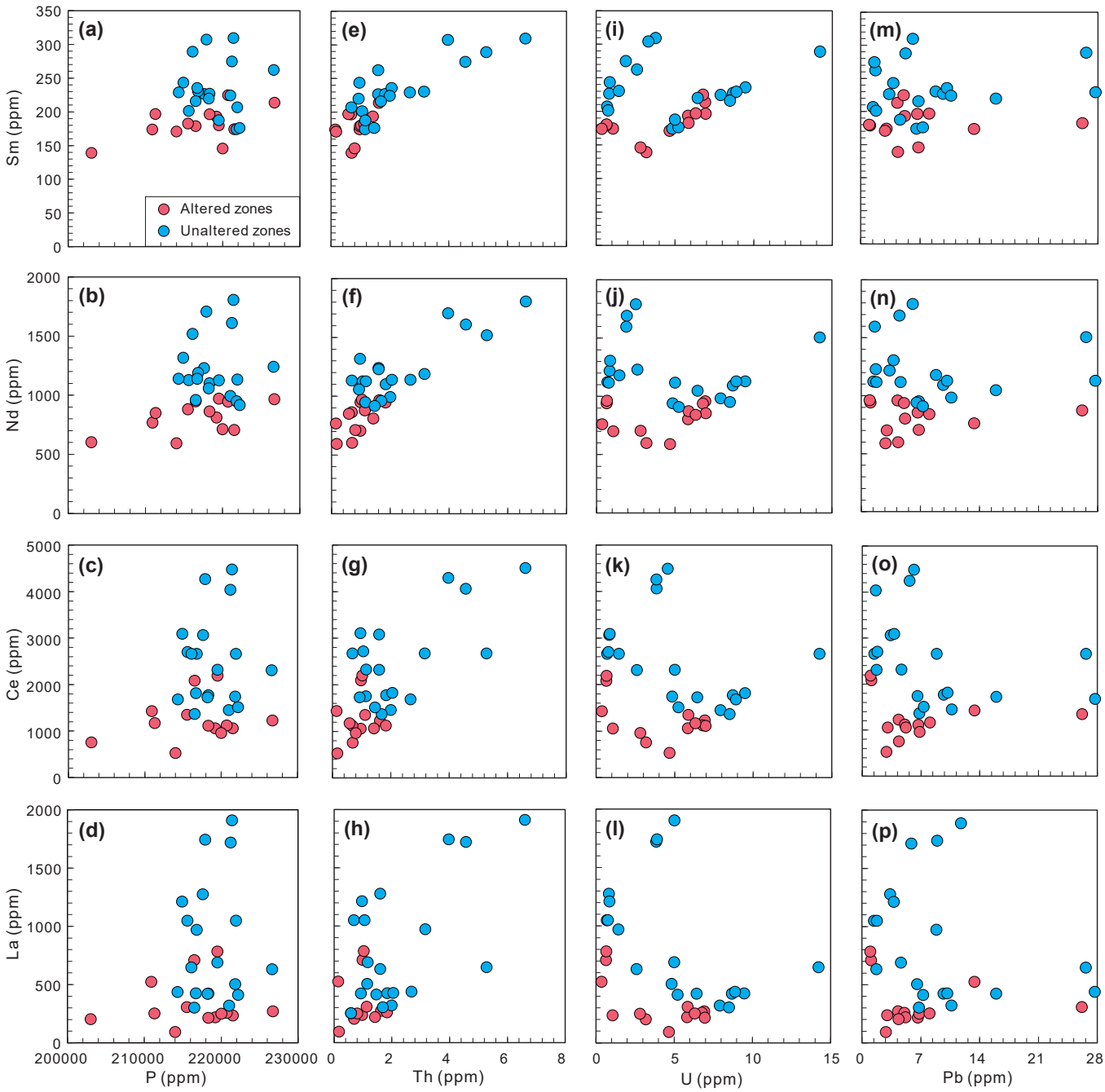

Figure 14

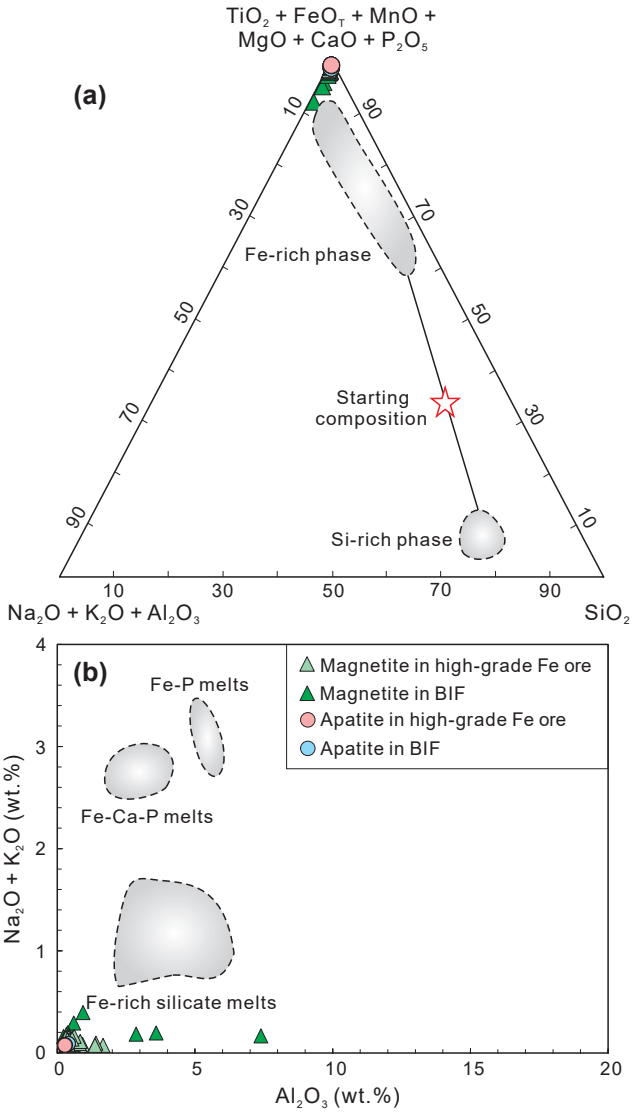

This is the peer-reviewed, final accepted version for American Mineralogist, published by the Mineralogical Society of America.
The published version is subject to change. Cite as Authors (Year) Title. American Mineralogist, in press.
DOI: https://doi.org/10.2138/am-2022-8525. http://www.minsocam.org/

Figure 15